

# Small-Signal Model for Inhomogeneous Helix Traveling-Wave Tubes using Transfer Matrices

Robert Marosi,<sup>1</sup> Kasra Rouhi,<sup>1</sup> Tarek Mealy,<sup>1</sup> Alexander Figotin,<sup>2</sup> and Filippo Capolino<sup>1,\*</sup>

<sup>1</sup>*Department of Electrical Engineering and Computer Science,  
University of California, Irvine, Irvine, California, 92697*

<sup>2</sup>*Department of Mathematics, University of California, Irvine, Irvine, California, 92697*

(Dated: October 17, 2024)

We introduce a practical method for modeling the small-signal behavior of frequency-dispersive and inhomogeneous helix-type traveling-wave tube (TWT) amplifiers based on a generalization of the one-dimensional Pierce model. Our model is applicable to both single-stage and multi-stage TWTs. Like the Pierce model, we assume that electrons flow linearly in one direction, parallel and in proximity to a slow-wave structure (SWS) which guides a single dominant electromagnetic mode. Realistic helix TWTs are modeled with position-dependent and frequency-dependent SWS characteristics, such as loss, phase velocity, plasma frequency reduction factor, interaction impedance, and the coupling factor that relates the SWS modal characteristic impedance to the interaction impedance. For the multi-stage helix TWT, we provide a simple lumped element circuit model for combining the stages separated by a sever, or gap, which attenuates the guided circuit mode while allowing the space-charge wave on the beam to pass freely to the next stage. The dispersive SWS characteristics are accounted for using full-wave eigenmode simulations for a realistic helix SWS supported by dielectric rods in a metal barrel, all of which contribute to the distributed circuit loss. We compare our computed gain vs frequency, computed using transfer matrices, to results found through particle-in-cell (PIC) simulations and the 1D TWT code LATTE to demonstrate the accuracy of our model. Furthermore, we demonstrate the ability of our model to reproduce gain ripple due to mismatches at the input and output ports of the TWT.

## I. INTRODUCTION

For decades, traveling-wave tubes (TWTs) have been essential for applications which require high-power, broadband amplification at microwave and millimeter-wave frequencies. These applications include, but are not limited to radar, telecommunication, and electronic warfare. Traveling-wave tube amplifiers are highly reliable, long lasting, and efficient in their niche high frequency, high bandwidth, and high power applications, compared to their solid-state power amplifier counterparts [1]. The basic TWT amplifier is composed of a slow-wave structure (SWS) and a confined linear electron beam which flows in close proximity to the SWS. The guided modes that propagate in the SWS in the presence of the electron beam make the TWT a distributed amplifier by converting the kinetic energy of the electron beam into amplified waves when both the beam and the guided waves are velocity synchronized [2, 3]. There are various types of SWS geometries for TWTs, though the one we consider here is the most common type: the tape helix. Helix-type TWTs can efficiently amplify waves over bandwidths of one octave and higher at moderate power levels, primarily limited by their capability to dissipate heat [4]. Some notable examples of helix-type satellite TWTs with high efficiencies, long lifetimes, and moderate bandwidths can be found in Refs. [1, 5–9]. Various wide bandwidth helix-type TWTs for applications such as electronic warfare have also been showcased in Refs. [1, 10–12].

To amplify waves to power levels on the order of 100 Watts without needing a high-power input signal, a large power gain is required for such TWTs. Traveling-wave tubes can be made to exhibit large small-signal power gain by either increasing the Pierce gain parameter,  $C$  (e.g., increasing the electron beam current), or by increasing the number of electronic wavelengths,  $N$ , in the structure (i.e., increasing the number of unit cells,  $N_c$ , in the periodic structure)[3]. However, to keep the TWT stable against backward wave and regenerative oscillations at frequencies where the small-signal gain is high, it is sometimes necessary to separate high-gain TWTs into sections, or stages, separated by severs. The purpose of the sever is to isolate TWT stages such that the guided electromagnetic (EM) wave cannot propagate to the next stage but the space-charge wave supported by the electron beam is allowed to pass and continue to be modulated in the next stage. This way, the reflected waves at the output stage of the TWT cannot return all the way to the input of the structure and be re-amplified. A typical rule-of-thumb for practical helix TWT designs is to have no more than 20 dB of gain per stage in TWTs to minimize nonlinearities and minimize the risk of regenerative oscillations [13, (Ch. 12)]. Furthermore, practical helix TWTs are often inhomogeneous in pitch along the tube length. For example, in order to improve the matching of the helix circuit to coaxial input/output terminations on the TWT, pull-turns (i.e. increasing helix pitch at the input/output ends of the helix) may be added to the tube, as long as the length of the pitch transition is long with respect to the guided wavelength [14, (Ch. 12)]. Additionally, to increase the available saturation power

\* f.capolino@uci.edu

and enhance the beam-wave power conversion efficiency of the TWT, pitch tapers may be added along the length of the helix. The purpose of the taper is to maintain velocity synchronization between the beam and guided waves as the mean velocity of the beam is reduced at the end of the tube, as explained in [14, (Ch. 10)] and in works such as in Refs. [15–19].

## II. PROBLEM STATEMENT

We develop a simple linear model to predict the small-signal gain of TWT amplifiers with helix-based SWSs. The linear model works for interaction regions that consist of either one stage (without a sever) or two stages separated by a sever as shown in Fig. 1(a). The sever in a two-stage helix TWT typically consists of a gap between the helix sections and a position-dependent attenuation on the dielectric support rods to suppress reflected EM waves. The two-stage helix SWS geometry has a geometric period  $d$  and  $N_{c,tot} = N_{c,1} + N_{c,2}$  unit cells, with  $N_{c,1}$  and  $N_{c,2}$  cells on stage 1 and 2, respectively. Furthermore, the helix SWS (either single-stage or two-stage) can also include position-dependent features such as phase velocity tapers and/or attenuators. The developed model accounts for the interaction between the space-charge waves of the electron beam (also accounting for the space-charge effects) and the EM wave guided by the SWS. Using this model, it is possible to determine the RF output power of the EM wave exiting the output port of the TWT ( $P_{out}$ ) for a given input RF power ( $P_{in}$ ) at the input port of the TWT, assuming that the TWT operates in the linear (small-signal) regime.

The model described here is based on the generalization of the Pierce model in [20]. However, unlike the works of [2, 3, 21] and the augmented model in [20], we make our model more general in several ways: by considering the dispersive coupling parameters as discussed in the next section, by modeling the EM properties of the sever gap of the helix SWS using a capacitive network, and by considering real TWT features that are not necessarily homogeneous along  $z$  (such as pitch tapering and distributed loss patterning). In Section III, we provide the analytical formulations for the system and transfer matrices, based on the generalized Pierce model, that can be used to model discretized segments of the “hot” TWT (i.e., with the electron beam present inside the SWS) as homogeneous equivalent transmission lines. A more detailed formulation can be found in [20, 22]. Furthermore, we highlight that the model shown in this work is compatible with TWTs with SWSs other than the helix geometry. For instance, ref. [22] demonstrates this linear model for a serpentine TWT, albeit without losses or position-dependent features. However, we restrict our discussion to the single-stage and two-stage helix-type TWT with arbitrary position-dependent loss distributions.

Using the unit cell dimensions provided in Section IV, we explain how the interaction impedance and attenu-

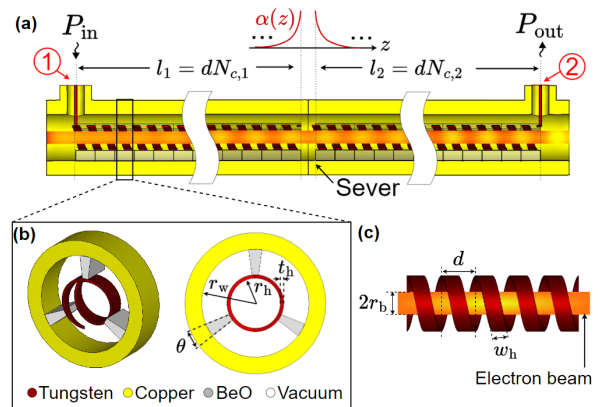


Figure 1: (a) TWT interaction region: full-length two-stage SWS with electron beam, sever and position-dependent attenuation. The electron gun and collector are not shown here. For simplicity, windows have not been included at the input or output ports of the structure. Input and output ports 1 and 2, respectively, are labeled with red circles. (b) Isometric and front views of a single unit cell of the SWS composed of a tungsten tape helix supported by three equidistant BeO dielectric rods within a circular copper waveguide. (c) Horizontal view of the tape helix SWS with cylindrical electron beam flowing through the center of the SWS.

ation coefficient used in our generalized Pierce model are computed using results from the eigenmode solver of the commercial software CST Studio Suite in Section V. In Section VI, we explain how we construct the equivalent transfer matrix for single-stage and two-stage helix TWTs. Then, in Section VII, we explain how we compute the small-signal gain and evolution of the state vector for the TWT examples, considering an equivalent lumped circuit network at the sever and terminations at the input/output ports of the TWT. Since our model relies on equivalent transmission lines (TLs) and load impedances, it allows us to observe how mismatches at the input and output ports of the TWT lead to gain ripple. In Section VIII, we show the gain vs frequency and evolution of the state vector versus position for the TWT examples and compare the results of our model to those from particle-in-cell (PIC) simulations and to those from the 1D TWT code LATTE. Finally, in Section IX, we explain how our model differs from the TWT code LATTE.

## III. GENERALIZED PIERCE MODEL

To model TWTs that are inhomogeneous along their length, we segment each TWT stage of length  $l$  into  $S$  segments of *homogeneous* equivalent transmission lines

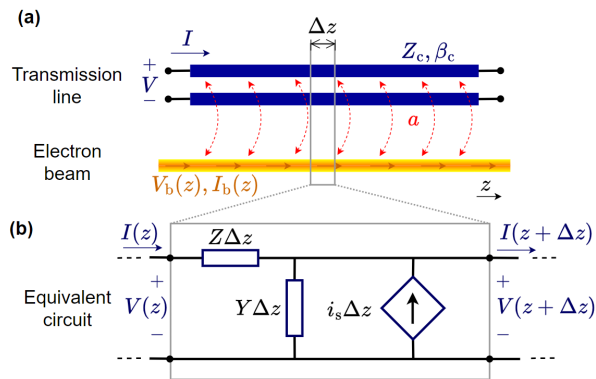


Figure 2: (a) Section of an equivalent transmission line of characteristic impedance  $Z_c$  and cold propagation constant  $\beta_c$  coupled to an electron beam through the coupling parameter  $a$ . (b) Equivalent per-unit-length circuit of transmission line with distributed impedance  $Z$  and admittance  $Y$ , with current-dependent “source” current generator  $i_s = -a(dI_b/dz)$  to account for the effect of the electron beam on the guided EM wave.

(i.e. each segment has a constant attenuation, phase velocity, and characteristic impedance), similarly to what has been done in [23]. The homogeneous equivalent transmission line model for a segment of the TWT stage is illustrated in Fig. 2. The homogeneous transmission line segments for each stage have a fixed length of  $\Delta l = l/S$ , where  $S$  is the number of segments. Note that in this paper,  $S$  does not need to be equal to the number of unit cells in the SWS,  $N_c$ , which allows for more flexibility in the modeling of non-homogeneous parameters along the SWS. In the prior work by Rouhi et al. [22], the TWT was partitioned into segments with length equal to the period of the serpentine waveguide unit cell (i.e.,  $\Delta l = d$  and  $S = N_c$ ). Specifically, subdividing the TWT stages by the geometric period of the SWS,  $d$ , works well for TWTs with no position-dependent features along their length. TWTs with pitch tapering and/or loss patterning sometimes need to be modeled with more transmission line segments than the number of unit cells (i.e.  $\Delta l < d$ ) in order to adequately resolve these features (e.g. TWTs with loss patterning near the sever that rapidly varies from one unit cell to the next). Table I summarizes the important parameters used to subdivide the TWT stages and define their physical length in our model (the subscripts 1 and 2 are later introduced to denote the parameters for the first and second stages in a two-stage TWT, respectively, in Sec. VI).

Pierce theory is often used to describe the interaction between the space-charge waves of an electron beam and the guided EM mode using equivalent transmission lines in the small-signal regime with linearized equations. In Pierce theory, the TWT system is considered as a one-dimensional problem, with a guided EM wave on a SWS interacting with a linear space- and time-varying elec-

Table I: Parameters used to describe the length of each TWT stage and its segments.

Parameter	Description	Notes
$d$	Geometric period of the unit cell	
$N_c$	Number of unit cells in a TWT stage	
$l$	Length of a TWT stage	$l = N_c d$
$S$	Number of homogeneous segments	
$s$	Segment index	$s = 1, 2, \dots, S$
$\Delta l$	Length of a segment in a TWT stage	$\Delta l = l/S$

tron beam confined by a strong axial magnetic field, such that only electron movement in the axial ( $+z$ ) direction is considered. For simplicity, we also assume that the axial electric field of the modes guided by the SWS and acting on the electron beam is approximately uniform over the cross-section of the electron beam, as was done in [2, 3, 20, 21]. The electron beam has an average equivalent kinetic voltage  $V_0$  and average beam current  $-I_0$  in the  $+z$  direction (using conventional flow notation, positive values of  $V_0$  and  $I_0$  are used in the remainder of this paper). The average axial velocity of electrons in the beam is  $u_0$  and it is approximately related to the average kinetic voltage as  $V_0 \approx u_0^2/(2\eta)$  for low-voltage beams (i.e. for  $V_0$  near 10 kV or below [24]), where  $\eta = e/m_0 = 1.7588 \times 10^{11}$  C/kg is the charge-to-rest-mass ratio of an electron. Note that this approximation for the electron kinetic voltage-velocity relation is needed, since the equations of the generalized Pierce model used here are derived using that approximation [20]. For higher beam voltages, it is necessary to account for changes in the effective electron mass in the derivation of the electron beam equations of [20]. Development of a generalized Pierce model with relativistic corrections is planned for a future paper. Hence, we limit our generalized Pierce model in this work to the non-relativistic regime, as it builds upon our previous works (which were also formulated using non-relativistic equations) [20, 22, 25–27]. The EM-charge modes that exist when the guided EM wave interacts with the electron beam are sometimes called “hot” modes, whereas passive EM modes guided by the SWS without the electron beam are called “cold” modes. For brevity, only the final equations necessary for the Pierce model are shown in this section. Detailed derivations of the equations governing the Pierce model may be found in the original Pierce papers [2, 3, 21], or in [20] and its supplementary material. Here, we augment the generalized Pierce model of [20, 22] to include inhomogeneous features over the length of the TWT.

The equivalent transmission line model for a homogeneous TWT segment is illustrated in Fig. 2(b). Under the small-signal, nonrelativistic approximations of the Pierce model, the four differential equations governing the dynamics of the electron beam and equivalent transmission line in the phasor domain can be repre-

sented in a compact matrix form at each frequency  $\omega$  and longitudinal position  $z$  along the circuit, with implicit  $\exp(j\omega t)$  dependence,  $\frac{d}{dz}\Psi(z) = -j\mathbf{M}_s\Psi(z)$ , with  $z \in [(s-1)\Delta l, s\Delta l]$ , where the subscript  $s = 1, \dots, S$  is the index corresponding to each segment along each stage of the TWT, the position-dependent  $4 \times 1$  state vector

$$\Psi(z) = \begin{bmatrix} V(z), I(z), V_b(z), I_b(z) \end{bmatrix}^T, \quad (1)$$

represents the modulated voltage and current phasors on both the beam ( $V_b$  and  $I_b$ ) and the SWS ( $V$  and  $I$  representing the guided electric and magnetic fields along the SWS as equivalent voltages and currents, respectively [20, 28, 29]), with T as the transpose operator. In our examples, we define the voltage,  $V$ , as the potential difference between the surface of a conducting sheath helix and surrounding metal walls and we define the current,  $I$ , as the longitudinal component of current along the sheath helix. The sheath model we use is explained in detail in Refs. [30, 31] and in Appendix A. By using the sheath helix model, we are able to treat each SWS segment as a uniform transmission line, even when the segment length  $\Delta l$  is smaller than the physical period of the unit cell,  $d$ . The  $4 \times 4$  system matrix  $\mathbf{M}_s$  is homogeneous for each segment of the TWT

$$\mathbf{M}_s = \begin{bmatrix} 0 & k_c Z_c & 0 & 0 \\ k_c/Z_c & 0 & -ag & -a\beta_0 \\ 0 & ak_c Z_c & \beta_0 & \zeta_{sc} \\ 0 & 0 & g & \beta_0 \end{bmatrix}. \quad (2)$$

In Eqn. (2),  $k_c = \beta_c - j\alpha_c$  is the ‘‘cold’’ complex circuit wavenumber, that also accounts for losses in the SWS, and  $Z_c = V^+/I^+$  is the characteristic impedance of a given transmission line segment,  $s$ , in terms of the forward voltage and current waves traveling in the positive  $z$ -direction, denoted by the  $+$  sign (The total voltage and current in the presence of reflections is the sum of forward-traveling and backward-traveling waves, i.e.  $V(z) = V^+(z) + V^-(z)$  and  $I(z) = I^+(z) + I^-(z)$ , see Ref. [32, (Ch. 2)]). Note that both the characteristic impedance and propagation constant in the matrix above can vary from segment to segment due to effects such as pitch tapering and position-dependent attenuation. For brevity, segment indices are not included in the subscripts for  $k_c$  and  $Z_c$ . The definition of voltage and current on the helix SWS is chosen to yield the net EM power as  $P = \frac{1}{2}\text{Re}(VI^*)$ , where the asterisk (\*) denotes complex conjugation. Here, we use the sheath helix model from [30, 31] to define our helix voltage and current, and by neglecting losses in the sheath helix, we compute the resultant purely-real helix characteristic impedance  $Z_c$  in Appendix A (small losses are accounted for only by the complex propagation constant in our generalized Pierce model). Using a purely-real approximation for characteristic impedance and a complex propagation constant, is based on the simplifying assumption that the SWS is

a low-loss transmission line [33, (Ch. 4)][32, (Ch. 2)][34, (Ch. 5)]. The real part of the cold circuit wavenumber is related to the cold phase velocity of a segment (of length  $\Delta l = l/S$ , as explained above) of the low-loss SWS,  $v_c$ , as  $\beta_c = \omega/v_c$ . Whereas the imaginary part of the propagation constant,  $\alpha_c$  is the attenuation per unit length (in Nepers per meter) for guided waves on the SWS. For each homogeneous segment of the equivalent transmission line that represents the SWS, the quantities  $k_c Z_c$  and  $k_c/Z_c$  in Eqn. (2) are related to the equivalent per-unit-length distributed series impedance and shunt admittance, as  $Z = jk_c Z_c$  and  $Y = jk_c/Z_c$  respectively, as illustrated in Fig. 2(b). Furthermore, the average electronic phase constant is  $\beta_0 = \omega/u_0$ ,  $g = I_0\beta_0/(2V_0)$ , and  $\zeta_{sc} = 2V_0\omega_q^2/(\omega I_0 u_0)$ , as was also considered in [20, 22, 35]. Note that  $i_s$  from Fig. 2 is represented in Eqn. (2) as  $i_s = -a(dI_b/dz) = jagV_b + ja\beta_0 I_b$ . The frequency-dependent quantity  $\omega_q = R_{sc}\omega_p$  is the reduced plasma angular frequency of the electron beam, which is proportional to the plasma frequency  $\omega_p$  by the plasma frequency reduction factor  $R_{sc}$ . The formulas used for  $\omega_p$  and  $R_{sc}$  are provided in Appendix E. The frequency-dependent coupling coefficient  $a = (Z_P/Z_c)^{1/2}$  is a factor which relates the actual characteristic impedance of the EM mode guided by the SWS to the beam-EM mode interaction impedance (sometimes referred to as Pierce impedance), as derived in [22]. We also show, in Appendix B, that the system matrix  $\mathbf{M}_s$  may be transformed into  $\mathbf{M}'_s$  to be in terms of interaction impedance  $Z_P$  only (see Appendix B), without dependence on the coupling coefficient  $a$  or the characteristic impedance of the SWS  $Z_c$ . In the original work by Pierce [2, 3, 21], there was no distinction between these two impedances;  $Z_P$  was used as both the characteristic impedance and interaction impedance. However the equivalent voltages and currents on the transmission line for this transformed system matrix will also be scaled by  $a$ ; one must consider the power of the guided mode when using the transformed model, rather than the helix voltage (and characteristic impedance) that can be defined in multiple ways [36]. We note that, in this paper, the interaction impedance  $Z_P$  obtained by full-wave simulations is only used to determine the coupling coefficient  $a$ , unless one uses the alternative system matrix formulation provided in Appendix B. Generalized Pierce models using the coupling strength coefficient  $a$  have also been developed in [20, 22, 25–27], but unlike those previous works, here we consider the fact that the TWT can be lossy, dispersive, and inhomogeneous along its length. Furthermore, we demonstrate in Appendix F that the fourth-order modal dispersion relation from Pierce theory [2, 3][21, Ch. 2][37, Ch. 8] can be obtained using the system matrix of Eqn. (2), provided that the characteristic impedance  $Z_c$  is assumed equal to the interaction impedance  $Z_P$  (as is done in conventional Pierce theory) to make the coupling coefficient  $a$  equal to unity. We also note that, unlike with our model, the original works by Pierce did not consider dispersive parameters (e.g. frequency-dependent interaction

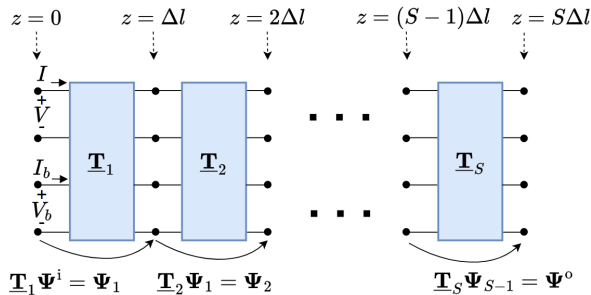


Figure 3: Cascading of 4-port transfer matrices to model the spatial evolution of the state vector with position along the TWT. Each transfer matrix  $\underline{\mathbf{T}}_s$  represents a segment of length  $\Delta l$  in the TWT.

impedance and phase velocity for the modes supported by the cold SWS) in solving for the modal dispersion relation for the TWT [2, 3, 21].

Realistic SWSs for TWTs are both dispersive and lossy, with position-dependent features such as pitch tapering and loss patterning. Because of this fact, the characteristic impedance  $Z_c$ , coupling factor  $a$ , and complex cold propagation constant  $k_c$  of the equivalent uniform transmission line segments can be position dependent and frequency dependent. The real and imaginary parts of the cold complex propagation constant  $k_c$  and the purely-real interaction impedance  $Z_P$  of the SWS are computed through full-wave eigenmode simulations with CST Studio Suite (or equivalent EM simulation software) for lossy and dispersive SWSs, as explained in Section V.

Transfer matrices are used to relate the state vector  $\underline{\Psi}_s = \underline{\Psi}(s\Delta l)$  from one homogenous segment to the next and track its evolution along the length of the TWT, as illustrated in Fig. 3, where the TWT is subdivided into  $S$  segments with segment indices  $s = 1, \dots, S$ , and

$$\underline{\Psi}_s = \underline{\mathbf{T}}_s \underline{\Psi}_{s-1}. \quad (3)$$

The transfer matrix  $\underline{\mathbf{T}}_s$  for each TWT segment in Eqn. (3) is computed from the system matrix in Eqn. (2) using matrix exponentiation

$$\underline{\mathbf{T}}_s = \exp(-j\underline{\mathbf{M}}_s \Delta l). \quad (4)$$

Note that  $\underline{\Psi}^i = \underline{\Psi}(z = 0)$  in Fig. 3 corresponds to the excitation state vector applied to the input-end of the TWT, whereas the state vector at the output end of the TWT is  $\underline{\Psi}^o = \underline{\Psi}_S$ . Using such transfer matrices, along with appropriate boundary conditions, we can compute the small-signal gain of non-homogeneous, single-stage or multi-stage TWTs at each frequency, as we will show later in Section VII.

#### IV. SWS UNIT CELL DIMENSIONS AND PARAMETERS

The unit cell used in our single-stage TWT and two-stage TWT examples is shown in Figs. 1(b) and 1(c). The tungsten tape helix (with conductivity  $\sigma = 1.89 \times 10^7$  S/m) has a tape thickness  $t_h = 0.102$  mm, a helix inner radius  $r_h = 0.744$  mm, and it is supported by three equidistant beryllium oxide (BeO) dielectric rods (with  $\epsilon_r = 6.53$  and intrinsic  $\tan(\delta) = 3.58 \times 10^{-4}$  at 9.3 GHz and 300 K [38], in the “clean” regions of the SWS that have no loss coating). Note however, that the value of the effective loss tangent in the central region of the finite-length SWS is position-dependent due to the attenuation patterning. This attenuation patterning is required to mitigate regenerative oscillations, as explained in Sec. VI. Furthermore, the loss tangent is assumed to be constant with respect to frequency in our full-wave time-domain simulations (for finding the scattering parameters of the finite-length SWS and for finding the gain of the TWT in PIC simulations). The dielectric rods subtend angles of  $\theta = 14.2^\circ$  within a circular copper waveguide of inner radius  $r_w = 1.60$  mm (with conductivity  $\sigma = 5.96 \times 10^7$  S/m). Furthermore, the tape helix has a tape width  $w_h = 0.51$  mm and helix pitch (unit cell period)  $d = 1.04$  mm. The radial thickness of the copper waveguide is not a critical parameter in full-wave eigenmode simulations, provided that it is much greater than the skin depth.

#### V. INTERACTION IMPEDANCE AND ATTENUATION COEFFICIENT OF THE SWS

Like in the work of [20, 22], the per-unit-length transmission line parameters for a homogeneous “cold” SWS (i.e. without an electron beam present) can be computed using frequency-dependent results from full-wave eigenmode simulations. With the dimensions and materials of the unit cell for the helix SWS provided in Sec. IV, we use the finite-element eigenmode solver of CST Studio Suite to evaluate the cold phase velocity,  $v_c(\omega)$ , and interaction impedance,  $Z_P(\omega)$ , of the guided mode of the fundamental space harmonic in the cold structure, like in [39–41]. However, we also consider the effect of per-unit-length loss,  $\alpha$ , in the SWS, which can also be determined from full-wave eigenmode simulations as described below. In Ref. [22], it was shown that the characteristic impedance of the SWS, regardless of what voltage and current definitions are used to define it, is related to the interaction impedance,  $Z_P$ , by the real-valued, scalar coupling coefficient  $a$ , as  $Z_c = Z_P/a^2$ . We show in Appendix B that the voltage and current of the state vector  $\underline{\Psi}(z)$  may be transformed to put the system matrix  $\underline{\mathbf{M}}_s$  in terms of the usual interaction impedance  $Z_P$  from Pierce theory, as also explained in [22] (accurate voltage and current definitions are important when calculating the power of the EM wave along the TWT using our

model, but the calculated gain will be the same regardless of what characteristic impedance is used, since it is a ratio of powers). In other words, the model can be used to obtain correct gain-vs-frequency results for any purely-real and positive characteristic impedance  $Z_c$ , as long as the coupling coefficient  $a$  is calculated using this chosen characteristic impedance  $Z_c$  and the proper interaction impedance  $Z_P$ . As mentioned in Section III, we compute the characteristic impedance of the SWS segments analytically by considering the helix as a lossless anisotropically-conducting sheath, with helix voltage and current definitions provided in Appendix A. By considering the SWS as a sheath helix, we are able to track how the state vector evolves continuously along the SWS length, rather than from cell-to-cell like was done in [22], though one can also obtain meaningful results with other voltage and current definitions for the helix SWS.

From Pierce theory, the interaction impedance is defined for the fundamental Floquet-Bloch spatial harmonic as

$$Z_P(\beta_c) = \frac{|E_z(\beta_c)|^2}{2\beta_c^2 P(\beta_c)}, \quad (5)$$

where  $\beta_c$  is the phase constant within the fundamental Brillouin zone, defined here as  $\beta_c d/\pi \in [-1, 1]$ . For a helix-type TWT, the interaction impedance is typically evaluated within the fundamental Brillouin zone, where the beam-wave interaction is desired to occur. However, for space harmonic SWSs, such as the serpentine waveguide or coupled-cavity structure, one must consider higher order space harmonics when determining interaction impedance, like for the serpentine-type TWT studied in [22]. Furthermore,  $|E_z(\beta_c)|$  is the magnitude of the axial electric field phasor (i.e., the  $z$ -component), for a given phase constant, along the center of the SWS where the electron beam will be introduced, and  $P(\beta_c)$  is the time-average total power flux of the mode propagating through the SWS [42, (Ch. 10)]. The quantity  $|E_z(\beta_c)|$  is calculated from full-wave eigenmode simulations [43–45] as

$$E_z(\beta_c) = \frac{1}{d} \int_0^d E_z(z, \beta_c) e^{j\beta_c z} dz. \quad (6)$$

Conveniently, the EM energy simulated within the unit cell between periodic boundaries in the eigenmode solver of CST Studio Suite is always normalized to 1 Joule for each eigenmode solution. Thus, the time average power flux may be simply calculated as  $P = (1 \text{ Joule}) v_g/d$ , where the group velocity  $v_g = d\omega/d\beta_c$  can be determined directly from the dispersion diagram using numerical differentiation. Note that the eigenmode solver of CST Studio Suite neglects losses when finding the wavenumbers and EM fields of eigenmodes, so the electric field and wavenumbers used for computing the interaction impedance also neglect the effect of losses.

An approximation of the per-unit-length frequency-dependent cold attenuation coefficient (in Nepers/meter) is obtained from full-wave eigenmode simulations using the method developed in [46] as

$$\alpha_c \approx \frac{\omega}{v_g} \frac{1}{2Q}, \quad (7)$$

where  $Q$  is the frequency-dependent quality factor obtained from post-processing steps in the full-wave eigenmode solver of CST Studio Suite. The quality factor calculated from the eigenmode solver accounts for time-average volume and surface losses in the dielectric and metal materials as  $P_D = \pi f \varepsilon \iiint_V \tan(\delta) |\mathbf{E}|^2 dv$  and  $P_W = \frac{1}{2} \sqrt{\frac{\pi \mu f}{\sigma}} \iint_S |\mathbf{H}_{\tan}|^2 ds$  respectively, where  $f$  is the simulation frequency,  $\sigma$  is the conductivity of the metal,  $\varepsilon$  is the permittivity of the dielectric support rods,  $\tan(\delta)$  is the position-dependent loss tangent of the dielectric support rods,  $V$  is the volume of the dielectric support rods, and  $S$  is the surface of each conductor in these two equations only. The time-average power dissipated in the unit cell is  $P_{\text{loss}} = P_W + P_D$ , and the quality factor is  $Q = 2\pi f W/P_{\text{loss}}$ , where  $W$  is the total EM energy in the unit cell (for the eigenmode solver of CST, the fields are normalized such that  $W = 1$  Joule). Note that in our full-wave simulations, the loss tangent of the dielectric support rods is assumed to be independent of frequency. However, the attenuation coefficient  $\alpha_c$  is still frequency-dependent due to the dispersive fields and surface currents in the SWS. The conductivity, loss tangent, and relative permittivity of each material used in our examples is provided in Sec. IV. Position-dependent losses are implemented by scaling the loss tangent of the dielectric support rods as we will explain in detail in Section VI. Dielectric losses scale linearly with the loss tangent. However, the attenuation coefficient of Eqn. (7) ultimately depends on both metal losses and dielectric losses. Thus, the attenuation coefficient cannot be considered directly proportional to the loss tangent unless the metal losses are negligibly small with respect to the dielectric losses.

To implement losses in our generalized Pierce model and compute the equivalent per-unit length transmission line parameters, we assume that the “cold” guided wavenumber,  $k_c = \beta_c - j\alpha_c$ , of the SWS is complex, while using a purely-real characteristic impedance  $Z_c$  that is computed for a lossless sheath helix using the formulas shown in Appendix A. Since the interaction impedance  $Z_P$  is also purely real by definition, using a purely-real characteristic impedance conveniently results in a real and positive value for the coupling coefficient  $a$ .

The phase velocity, characteristic impedance, and interaction impedance versus frequency for the uniform-pitch structure shown in Fig. 1, with dimensions provided in Sec. IV, are shown in Fig. 4. The frequency- and position-dependent attenuation coefficient is described in detail in Appendix C. Note that scaling the coupling coefficient,  $a$ , will primarily shift the amplitude of the



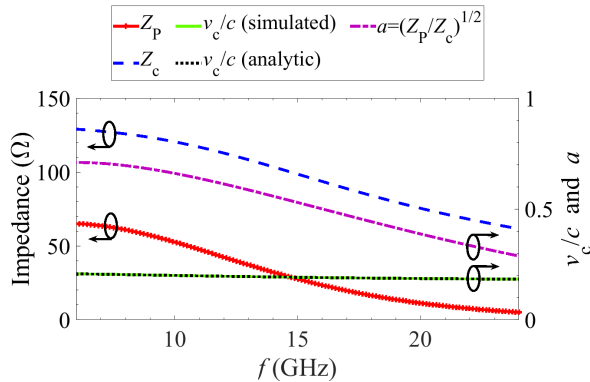


Figure 4: Interaction impedance, characteristic impedance, normalized phase velocity, and coupling coefficient  $a$  as a function of frequency for the helix SWS shown in Fig. 1 with dimensions provided in Section II. The phase velocity from the eigenmode solver from CST Studio Suite is compared to the analytical phase velocity computed using the sheath helix model in Appendix A, in good agreement.

peak gain, whereas scaling the plasma frequency reduction factor,  $R_{sc}$  (by changing the beam radius, helix inner radius, or electronic phase constant), will shift the frequency where the gain peak occurs.

## VI. CONSTRUCTION OF TWT TRANSFER MATRICES

As illustrative examples, we show how we build the transfer matrices in two simple TWT configurations: (i) a single-stage helix TWT with uniform pitch (i.e., uniform phase velocity and interaction impedance with position) and nonuniform loss patterning along its length, and (ii) a two-stage helix TWT with a sever between stages, uniform helix pitch on both stages, and nonuniform loss patterning. The commonly-used Gaussian and exponential loss patterns for each example are defined analytically in Appendix C. The loss patterns are used to attenuate reflected waves to mitigate the risk of regenerative oscillations. In practice, position-dependent attenuation is typically introduced to the helix SWS by coating the dielectric support rods with carbon via pyrolysis, with a thicker carbon coating near the center of the sever region [47, 48]. This loss coating can be represented in PIC simulations as an effective loss tangent in the bulk dielectric material of segmented dielectric rods. In the examples below, the loss pattern essentially involves three parameters. The *first*,  $\alpha_{\min}$ , is the the minimum attenuation coefficient along the SWS due to intrinsic dielectric and metal losses. The *second*,  $\alpha_{\max}$ , is the maximum attenuation coefficient along the SWS which is obtained by multiplying the the dielectric loss tangents of the dielec-

tric support rods by a scaling factor  $\tau$  (see Appendix C). Alternatively, one may select a suitable  $\alpha_{\max}$  based on our model, and then work backwards to determine the effective loss tangent corresponding to the desired maximum attenuation coefficient, provided that the TWT is stable and has an acceptable small-signal gain in the PIC simulations. This effective loss tangent corresponds to the lossy regions of the SWS that are heavily coated in carbon. The *third* parameter is the effective length of the loss pattern  $l_{\alpha}$ , which is associated to the full width half maximum (FWHM) of a Gaussian-shaped loss pattern (for the single-stage TWT) or the effective length for an exponential-shaped loss pattern (for the two-stage TWT), corresponding to the distance at which the attenuation coefficient falls below 1% of its maximum.

### A. Single-Stage TWT Transfer Matrix

Our first example structure, the single stage TWT, is composed of a uniform-pitch helix SWS with  $N_c = 95$  turns (SWS length  $l = N_c d = 98.8$  mm), with unit cell dimensions shown in Fig. 1 and described in Section II. Note again that, in our examples, the number of unit cells,  $N_c$ , is different from the number of segments,  $S$ , that the TWT stage is divided into to make the model more flexible. Based on the specific loss profiles shown in Appendix C, we implement a nonuniform position-dependent Gaussian-shaped loss pattern in our full-wave PIC simulations by setting a loss tangent for the dielectric support rods in each individual segment (with segment length  $\Delta l$ , as described above) along the length of the SWS, as explained in Appendix C. At the port-ends of the SWS, the loss pattern for the single-stage SWS has a frequency-dependent attenuation coefficient of  $\alpha_c = \alpha_{\min}$  (calculated using Eqn. (7)). At the midpoint between the input and output ports (i.e., at  $z = l/2$ ) the SWS has a frequency-dependent peak attenuation coefficient  $\alpha_{\max} = 80\alpha_{\min}$  (determined by scaling the dielectric loss tangent by a dimensionless factor of  $\tau = 2000$ ), and an effective loss pattern length of  $l_{\alpha} = 30$  mm, equal to the FWHM of the Gaussian function, as is explained in Appendix C. The quantities  $\alpha_{\min}$  and  $\alpha_{\max}$  correspond the attenuation coefficients in the “clean” and “deep” regions of the loss-coated dielectric support rods, respectively (i.e., the “clean” region of the rod has little-to-no carbon coating, whereas the “deep” region has the thickest coating of carbon [49, 50]). In our PIC simulations, using CST Studio Suite, we scale the loss tangent of the dielectric rods between  $\tan(\delta)$  and  $2000 \tan(\delta)$ , corresponding to  $\alpha_{\min}$  and  $\alpha_{\max}$ , respectively, using the position-dependent Gaussian profile mentioned above. The loss tangent values used in CST Studio Suite are sampled at a single frequency of 9.3 GHz, see Sec. IV. In the CST simulations, the loss tangent at each position is assumed to be constant with respect to frequency, which is a reasonable approximation over the desired operating frequency range.

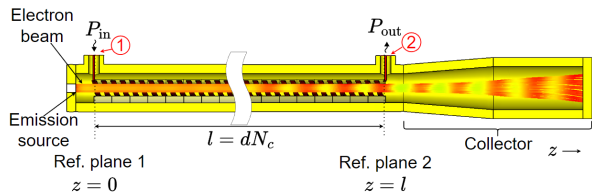


Figure 5: Slow-wave structure, emission source, electron beam, collector, and pin-to-helix transitions for a single-stage helix TWT. Electron bunches become denser along the SWS length due to beam-wave interaction. Reference planes for the TL model are indicated at  $z = 0$  and at  $z = l$ , between the two pin-to-helix connection points.

The single-stage TWT structure is discretized into  $S = 200$  homogeneous segments of length  $\Delta l = l/S$ . The attenuation coefficient, phase velocity, and characteristic impedance of the SWS are sampled along the length of the TWT, where the discrete axial positions along the TWT are defined using  $z = s\Delta l$ , where  $s = 1, \dots, S$ . The location  $z = 0$  corresponds to the start of the helical SWS at the input port of the TWT (port 1), where an input signal is applied, as illustrated in Fig. 5. Using these sampled data, one can obtain an equivalent system matrix  $\underline{\mathbf{M}}_s$  defined in Eqn. (2), and an equivalent transfer matrix  $\underline{\mathbf{T}}_s$  calculated from Eqn. (4) for each discrete position along the TWT. To construct the equivalent transfer matrix of the full SWS coupled to the electron beam, the transfer matrices of each discrete uniform segment of the TWT are cascaded using left multiplication as

$$\underline{\mathbf{T}} = \underline{\mathbf{T}}_S \dots \underline{\mathbf{T}}_2 \underline{\mathbf{T}}_1. \quad (8)$$

For our example, the scattering parameters of the cold single-stage TWT, determined from the time-domain solver of CST Studio Suite, indicate a reflection coefficient below -10 dB and a transmission coefficient well below -20 dB (due to attenuation) over the chosen operating frequency range, as shown in Fig. 6, allowing the input and output ports to be well-matched with good isolation to mitigate backward wave and/or regenerative oscillations. The discrepancies between the  $S_{21}$  of our TL model (with the coupling coefficient  $a = 0$  in the system matrix of each segment) and the simulated  $S_{21}$  (with loss patterning) in Fig. 6 are due to the fact that the TL model does not consider the effect of pin-to-helix transitions that are present in full-wave simulations. The TL model describes the interaction region between reference plane 1 that exists just after the pin-to-helix connection at the input port and reference plane 2 just before the pin-to-helix-connection at the output port, as illustrated in Fig. 5.

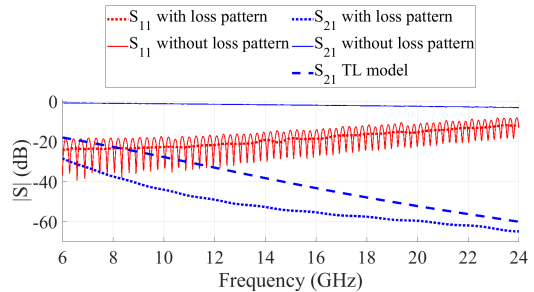


Figure 6: Scattering parameters of the single-stage TWT simulated in the time-domain solver of CST with and without attenuation patterning. The  $S_{21}$  of the cold TWT from our TL model (generalized Pierce model with no beam-wave coupling, i.e.,  $a = 0$ , and with a nonzero attenuation coefficient) is compared to the simulated  $S_{21}$  of the SWS with loss patterning. Note that the  $S_{11}$  for the TL model is not shown because it is on the order of  $-300$  dB due to matched terminations used in our examples (pin-to-helix transitions are not considered).

## B. Two-Stage TWT Transfer Matrix

Our second example structure, the two-stage TWT is composed of two uniform helix stages with  $N_{c,1} = N_{c,2} = 65$  turns ( $l_1 = l_2 = N_{c,1}d = N_{c,2}d = 67.6$  mm) with the same unit cell dimensions as we used in the previous example, as illustrated in Fig. 7. Note that the subscripts, 1 and 2 are introduced to the length parameters of Table I to indicate the first and second stages, respectively. The two helix stages are separated by a sever gap length of  $l_{\text{gap}} = 1$  mm. In this drift region (the sever gap illustrated in Fig. 7), there is an outer wall, but no helix or dielectric support rods. The attenuation pattern is exponential in shape leading into the sever for each helix stage, as explained in Appendix C, where  $\alpha_{\text{min}}$  is again calculated using Eqn. (7) and  $\alpha_{\text{max}} = 80\alpha_{\text{min}}$  (corresponding to a scaling of the rod loss tangent by a dimensionless factor of  $\tau = 2000$ ) at the edges of the sever gap (i.e. at positions  $z = l_1$  and  $z = l_1 + l_{\text{gap}}$ ). The effective loss pattern length (the length at which the attenuation decays from its maximum by a factor of  $e^{-5}$ , or less than 1%) on each helix stage is  $l_\alpha = 30$  mm.

Each TWT stage is discretized into  $S_1 = S_2 = 200$  homogeneous segments of lengths  $\Delta l_1 = l_1/S_1$  and  $\Delta l_2 = l_2/S_2$ , respectively. The scattering parameters of the two-stage cold TWT are shown in Fig. 8, which indicate an adequate match at the input and output ports, as well as adequate isolation between the ports. Again, the discrepancies between the scattering parameters of our TL model (with the coupling coefficient  $a = 0$ ) and the full-wave simulations of the scattering parameters (with loss patterning) in Fig. 8 are due to the fact that the TL model does not consider the effect of pin-to-helix tran-



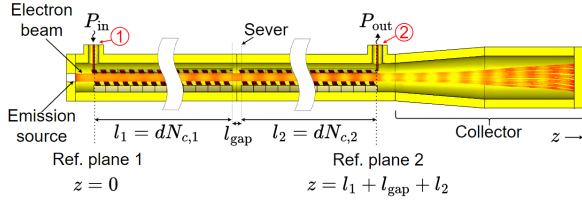


Figure 7: Slow-wave structure with sever gap, emission source, electron beam, collector and pin-to-helix transitions for a two-stage helix TWT. Electron bunching occurs along the SWS in both stages and bunches are unaffected by the sever gap. Reference planes for the TL model are indicated at  $z = 0$  and at  $z = l_1 + l_{\text{gap}} + l_2$ , between the two pin-to-helix connection points.

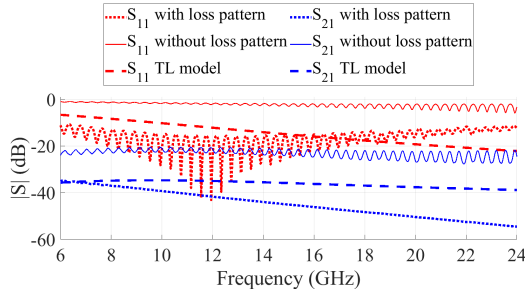


Figure 8: Scattering parameters of the two-stage TWT with and without attenuation patterning. The cold S-parameters of the transmission line model (with a lumped capacitive network to represent the sever gap, see Appendix D) are compared to the simulated S-parameters of the SWS with loss patterning.

situations that are present in full-wave simulations, as was also explained in the single-stage example. The input and output reference planes for the TL model are illustrated in Fig. 7 and are adjacent to the pin-to-helix connection points. We obtain an equivalent system transfer matrix for the input and output stages of the TWT, denoted by subscripts ST1 and ST2 respectively, by cascading the homogeneous transfer matrices  $\mathbf{T}_{1,s}$  and  $\mathbf{T}_{2,s}$  computed from Eqn. (4) in the forward direction (left multiplied) for each discrete position in each TWT stage for the input stage (bunching stage) as

$$\mathbf{T}_{\text{ST1}} = \mathbf{T}_{1,S_1} \cdots \mathbf{T}_{1,2} \mathbf{T}_{1,1}, \quad (9)$$

and similarly for the output stage (amplification stage) of the TWT

$$\mathbf{T}_{\text{ST2}} = \mathbf{T}_{2,S_2} \cdots \mathbf{T}_{2,2} \mathbf{T}_{2,1}. \quad (10)$$

However, even though an attenuation pattern is typically used to provide isolation between TWT stages, helix severers are still non-ideal; they reflect a large portion of

the RF wave (which is typically attenuated by loss patterning) and allow a small portion of the guided wave to traverse the sever gap due to capacitive coupling between helices. Thus, in our model, the RF transmission lines of stage 1 and 2 are connected using a two-port capacitive pi network with an ABCD matrix of  $\mathbf{T}_{\text{gap},c}$ , which describes the propagation of guided EM waves through the sever gap. The formulation of  $\mathbf{T}_{\text{gap},c}$  is provided in detail in Appendix D. Two port capacitive networks have also been used to represent center conductor discontinuities in coaxial transmission lines [51–53], which is a similar geometric configuration to the sever problem studied here. Note that, in the sever gap region, the RF wave is expected to be quite weak due to heavy distributed attenuation on either side of the sever gap. The resistive losses that can exist in the sever gap region are only due to RF wall currents and are neglected here because they are usually significantly smaller than the total losses on either side of the sever gap, and only capacitive coupling between helix stages is considered.

Next, for the beam portion of the sever gap, we use the transfer matrix

$$\mathbf{M}_{\text{gap},b} = \exp(-j\mathbf{M}_{\text{gap},b}l_{\text{gap}}) \quad (11)$$

that models how the space charge waves along the electron beam behave in the drift-space of the sever gap, like what was done in [54]. In the sever gap, there should be no coupling between the space charge wave and the EM guided mode, since there is no helix in the gap. From the beam equations in [20], we define the sever gap system matrix for the beam as

$$\mathbf{M}_{\text{gap},b} = \begin{bmatrix} \beta_0 & \zeta_{\text{sc,gap}} \\ g & \beta_0 \end{bmatrix}, \quad (12)$$

where  $\zeta_{\text{sc,gap}} = 2V_0\omega_{q,\text{gap}}^2/(\omega I_0 u_0)$  uses the reduced plasma angular frequency  $\omega_{q,\text{gap}} = R_{\text{sc,gap}}\omega_p$ . This reduced plasma frequency is computed as explained in Appendix E under the assumption that the radius of the metal wall in the sever gap is simply  $r_w$  instead of  $r_h$ . For convenience, the beam and capacitive gap transfer matrices are combined into one  $4 \times 4$  transfer matrix

$$\mathbf{T}_{\text{gap}} = \begin{bmatrix} \mathbf{T}_{\text{gap},c} & \mathbf{0}_{2 \times 2} \\ \mathbf{0}_{2 \times 2} & \mathbf{T}_{\text{gap},b} \end{bmatrix}, \quad (13)$$

where  $\mathbf{0}_{2 \times 2}$  is a  $2 \times 2$  matrix containing all zeros. Therefore, the total transfer matrix representing the two stages of the TWT is computed as

$$\mathbf{T} = \mathbf{T}_{\text{ST2}} \mathbf{T}_{\text{gap}} \mathbf{T}_{\text{ST1}}. \quad (14)$$

Next, we calculate the gain of both the single-stage and two-stage TWT examples by considering the source and load terminations (i.e., the boundary conditions) at the input and output of the TWT.

## VII. SOURCE AND LOAD TERMINATIONS

The effects of source and load impedances for both the single-stage and two-stage TWT examples are calculated by writing the equations for the boundary conditions. The elements of the state vector at the input and output of each stage are denoted by the superscript  $i$  and  $o$ , respectively.

Initially, the single-stage and two-stage TWTs in our TL model are terminated using matched source and load impedances at each frequency, i.e., we assume that  $Z_S = Z_L = Z_c$ . However, in PIC simulations and in reality, there are small reflections that occur between the helix SWS and input/output ports (e.g. pin-to-helix connection, RF windows, and external connections) which can make the device susceptible to oscillations if the TWT is conditionally stable, like with microwave transistor circuits [55, p. 217]. Therefore, we also study the effect of mismatches by considering source and load terminations that lead to a  $-10$  dB reflection coefficient at both ports of the TWT (i.e., we assume  $Z_S = Z_L = Z_c(1+\Gamma)/(1-\Gamma)$  with a  $\Gamma = 0.1$  that is constant with respect to frequency). When impedance mismatches are introduced at the TWT ports using our model, it is possible to observe rippling on the gain versus frequency and state vector versus position plots, as demonstrated in Sec. VIII.

For a single-stage TWT, the initial state of the beam and the input and output impedances on the ends of the beam lead to four equations that must be met at the input and output of the TWT,

$$\begin{cases} V_b^i = 0 \\ I_b^i = 0 \\ V^i + I^i Z_S = V_S \\ V^o - I^o Z_L = 0 \end{cases} \quad (15)$$

where the ac beam voltage and current are assumed to be zero at the electron-gun-end of the TWT and an ac voltage,  $V_S$  is applied to the input port of the TWT, as illustrated in Fig. 9. Similarly, for the two-stage TWT, as illustrated in Fig. 10, we have the following equations to represent the boundary conditions,

$$\begin{cases} V_{b,1}^i = 0 \\ I_{b,1}^i = 0 \\ V_1^i + I_1^i Z_S = V_S \\ V_2^o - I_2^o Z_L = 0 \end{cases} \quad (16)$$

These two sets of equations, together with  $\Psi^o = \underline{\mathbf{T}}\Psi^i$  and  $\Psi_2^o = \underline{\mathbf{T}}\Psi_1^i$  for the single-stage and the two-stage TWTs, respectively, lead to the  $8 \times 8$  matrix problem  $\underline{\mathbf{A}}\mathbf{x} = \mathbf{y}$ ,

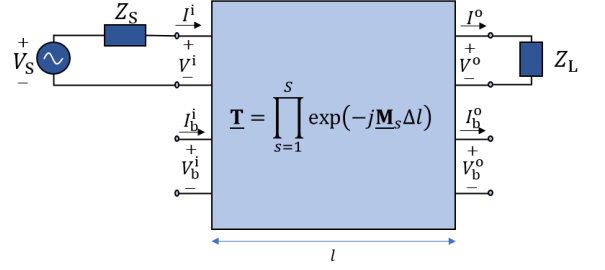


Figure 9: Circuit model used to compute the gain of a single-stage TWT of length  $l$ , terminated with source and load frequency-dependent impedance  $Z_S$  and  $Z_L$ , respectively, and driven with excitation voltage  $V_S$ .

Equivalent transfer matrix  $\underline{\mathbf{T}}$  computed by left-multiplying transfer matrices for discrete segments of transmission line, of length  $\Delta l$ .

for either TWT under consideration, where

$$\underline{\mathbf{A}} = \begin{bmatrix} -\underline{\mathbf{T}} & \underline{\mathbf{I}}_{4 \times 4} \\ 0 & 0 & 1 & 0 & 0 & 0 & 0 & 0 \\ 0 & 0 & 0 & 1 & 0 & 0 & 0 & 0 \\ 1 & Z_S & 0 & 0 & 0 & 0 & 0 & 0 \\ 0 & 0 & 0 & 0 & 1 & -Z_L & 0 & 0 \end{bmatrix}, \quad (17)$$

and  $\underline{\mathbf{I}}_{4 \times 4}$  is the  $4 \times 4$  identity matrix, and  $\underline{\mathbf{T}}$  is the  $4 \times 4$  total transfer matrix of either the single-stage or the two-stage TWT (given by Eqns. (8) and (14), respectively). Furthermore, the known vector of this system is

$$\mathbf{y} = [0, 0, 0, 0, 0, 0, V_S, 0]^T. \quad (18)$$

The unknown  $8 \times 1$  vector  $\mathbf{x}$  to be calculated, that describes the state vectors at both ends of the TWT, is

$$\mathbf{x} = [V^i, I^i, V_b^i, I_b^i, V^o, I^o, V_b^o, I_b^o]^T, \quad (19)$$

for the single-stage TWT, and

$$\mathbf{x} = [V_1^i, I_1^i, V_{b,1}^i, I_{b,1}^i, V_2^o, I_2^o, V_{b,2}^o, I_{b,2}^o]^T, \quad (20)$$

for the two-stage TWT.

Solving this  $8 \times 8$  system of equations for the state vector  $\mathbf{x}$  allows us to compute the transducer power gain of the single-stage TWT as  $G = P^o/P^i$ , where  $P^i = V_S^2/(8Z_S)$  is the available RF input power at the input port of the TWT (or power of the incident wave) and  $P^o = \frac{1}{2}\text{Re}(V^o I^{o*})$  is the RF output power delivered to the load at the output port of the TWT, and  $*$  indicates complex conjugation. Similarly, we calculate the transducer power gain of the two-stage TWT as  $G = P_2^o/P^i$ , where  $P_2^o = \frac{1}{2}\text{Re}(V_2^o I_2^{o*})$ .

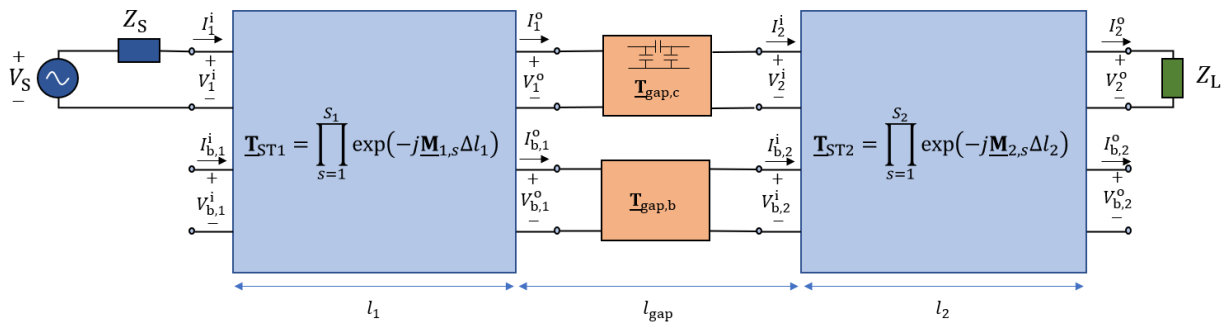


Figure 10: Circuit model used to compute the gain of a two-stage TWT. The input and output stages have lengths  $l_1$  and  $l_2$ , and the elements of their state vectors are denoted by the subscript 1 and 2, respectively. The sever gap transfer matrices of the TL circuit,  $\mathbf{T}_{\text{gap},c}$ , and of the beam,  $\mathbf{T}_{\text{gap},b}$ , represent the sever gap of length  $l_{\text{gap}}$  that separates the two helix stages.

### VIII. RESULTS: GAIN AND EVOLUTION OF THE STATE VECTOR

By applying the boundary conditions described in Sec. VII (one case with  $Z_S = Z_L = Z_c$  for perfect matching at the input and output port of the TWT at each frequency, and another case with  $Z_S = Z_L = Z_c(1 + \Gamma)/(1 - \Gamma)$ , corresponding to a constant  $-10$  dB mismatch at both ports at each frequency, where  $\Gamma = 0.1$ ), we calculate the gain of our single-stage and two-stage TWT examples. The gain of the model described above for the example single-stage and two-stage TWTs is plotted against frequency in Figs. 11a and 12a, respectively. The gain of the model is compared to the gain found from CST PIC simulations and the open source TWT code LATTE [56] using the same dimensions and parameters as the analytic generalized Pierce model. The PIC setups for the single-stage and two-stage TWTs are shown in Figs. 5 and 7, respectively.

The single-stage and two-stage TWTs in our examples are designed to operate with a dc kinetic equivalent beam voltage of  $V_0 = 10.5$  kV ( $u_0 \approx 0.2c$ ) and dc beam current of  $I_0 = 50$  mA, with a beam radius of  $r_b = 0.46$  mm. For simplicity, we assume that the SWS in each example is immersed in a strong uniform axial magnetic field of  $B_z = 1$  T to confine the electron beam in our PIC simulations. The electron gun of the TWT in our PIC simulation is represented as a simple circular area source dc emission. The collector is a single-stage design, held at the same potential as the walls of the TWT. A single-tone sinusoidal input signal is applied to port 1 with a constant *accepted* input power of  $P_{\text{in}} = -10$  dBm at each simulated frequency. If the input termination of the TWT has an impedance mismatch, the available input power would be slightly larger than the accepted input power. This is an important detail to consider when examining the plots of the RF power on the SWS versus position.

The input power of  $-10$  dBm was selected to ensure linear operation for the TWT in PIC simulations, since our model builds on linearized small-signal equations like

in conventional Pierce theory [2, 3, 21]. We have verified in PIC simulations that an input power of  $-10$  dBm drives the TWT well below the 1 dB gain compression point [55, Ch. 4] for both TWT examples in this study. Larger input powers on the order of 30 dBm or higher, for example, may drive the TWT into the nonlinear saturation regime in reality and in full-wave PIC simulations; in the saturation regime, our small-signal model cannot accurately reproduce the results of full-wave PIC simulations and large-signal TWT codes such as LATTE should be used.

#### A. Single-Stage TWT

The single-stage TWT example was simulated using the PIC solver of CST Studio Suite with a simulation duration of 10 ns, approximately 21.3 million mesh cells, and approximately 1.86 million macroparticles. Also, we use PIC simulations to confirm that the TWT is zero-drive stable. In this example, the SWS of the TWT consists of  $N_c = 95$  unit cells. The peak gain of our model (with perfect matching at the input and output ports) is within approximately 0.9 dB of the peak gain found using PIC simulations. However, the frequency of the peak gain is shifted by approximately 0.4 GHz, as shown in Fig. 11a. Interestingly, the gain from LATTE and our model agree well below approximately 10 GHz, but the frequency and amplitude of the peak gain of our model agree better with CST PIC simulations, especially at frequencies above the frequency of peak gain (above 12 GHz). Using our model, the state vector was sampled at discrete positions along the TWT after being cascaded through transfer matrices, as illustrated in Fig. 3.

The power of the RF wave guided along the circuit,  $P(z) = \frac{1}{2} \text{Re}(V(z)I^*(z))$ , is plotted vs distance at an operating frequency of 12 GHz, with and without a  $-10$  dB mismatch at the TWT ports with our analytic model, as shown in Fig. 11b. Additionally, we plot the approximate RF power of the guided wave along the TWT

using data from electric field monitors in PIC simulations. These monitors are placed periodically along the center of the beam in the TWT (with period  $d$ ), between each unit cell. The approximate RF power using these field monitors is calculated from Eqn. (5) using the steady-state ac magnitude of the longitudinal electric field (rather than the fundamental spatial harmonic of  $E_z$ ) as  $P_{\text{PIC}} \approx |E_z|^2 / (2\beta_c^2 Z_P)$ . The approximate RF power found from PIC field monitors is reasonably close to the RF power calculated by our model at the collector-end of the TWT for two reasons: (i) the fundamental space harmonic of  $E_z$  carries more energy than any other space harmonic and is close to in magnitude to the average  $E_z$  integrated over the unit cell period in eigenmode simulations for the helix SWS, (ii) the growing wave becomes dominant over the other three wave solutions near the collector-end of the TWT [3, 21]. Note that the small dip in RF power on the SWS from 0 mm to 15 mm can be attributed to the “launching losses” of Pierce theory [3, 21], where the guided EM wave deposits power to the space charge wave to modulate it at the start of the tube.

When mismatches are present at the input and output ports of the TWT, it appears that the power of the RF wave at the output end of the TWT is larger than the RF output power for the matched TWT in Fig. 11b, but the gain plots with and without mismatches in Fig. 11a are quite similar. This apparent discrepancy is due to the fact that our power gain definition is the transducer power gain, which depends on the *available* input power for the terminated TWT, rather than the constant  $-10$  dBm accepted (i.e., input) power used in our examples. When there is a mismatch at the input port of the TWT, the available RF power  $P^i = V_S^2 / (8Z_S)$  will be higher than the accepted RF power. The RF output power delivered to the load impedance at the end of the TWT, however, is still calculated as  $P^o = \frac{1}{2} \text{Re}(V^o I^{o*})$  and is consistent with the RF power shown in Fig. 11b. Furthermore, in Appendix G, we show a modified example of a spatially homogeneous single-stage TWT with only intrinsic losses (i.e. losses associated to  $\alpha_{\text{min}}$ ) to demonstrate that the RF power vs position and gain vs frequency plots have a similar but not identical profiles to those found through the conventional three-wave theory used by Pierce for spatially uniform TWTs (which also neglects reflections and backward wave) [21, Ch. 9][37, Ch. 8].

## B. Two-Stage TWT

The two-stage TWT example was simulated using the PIC solver of CST Studio Suite with a simulation duration of 10 ns, approximately 29.9 million mesh cells, and approximately 2.27 million macroparticles. In this example, the input and output stages of the SWS each consist of  $N_{c,1} = N_{c,2} = 65$  unit cells. For this example, the peak gain of our generalized Pierce model (with perfect matching at the input and output ports) is also

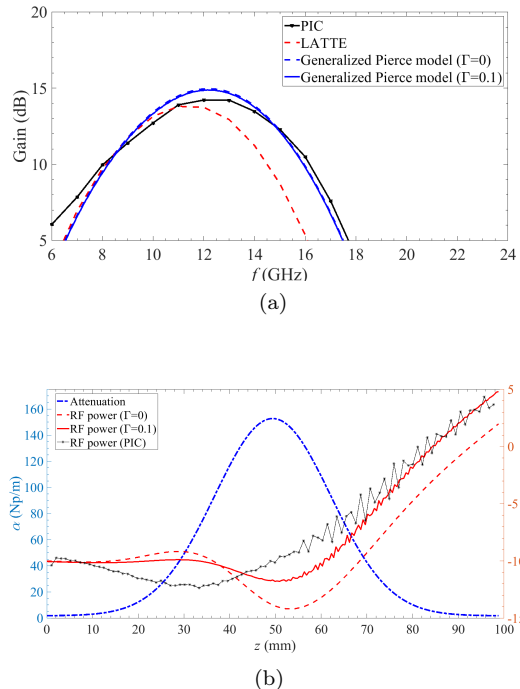


Figure 11: (a) Gain vs frequency for a single-stage TWT with no mismatches on both ports ( $\Gamma = 0$ , dashed blue line), and with a  $-10$  dB reflection on both ports ( $\Gamma = 0.1$ , solid blue line) calculated using model described in this paper and compared to PIC and LATTE simulations. (b) Plot of attenuation coefficient and calculated RF power along the SWS versus longitudinal position at 12 GHz with and without a  $-10$  dB mismatch (dashed red and solid red lines, respectively) at the TWT ports using our generalized Pierce model, in addition to the approximate RF power calculated from field monitors in PIC simulations (black line with dots).

within approximately 0.9 dB of the peak gain found using PIC simulations, with the frequency of the peak gain for our model approximately 0.7 GHz higher than the peak gain frequency found from PIC simulations, as shown in Fig. 12a. The frequency of the peak gain calculated from LATTE was approximately 0.5 GHz below the peak gain obtained through PIC simulations, but the peak gain agrees within approximately 0.6 dB with our PIC simulations. Furthermore, the gain-versus-frequency profile of our model consistently overshoots the gain from PIC simulations at frequencies above 13 GHz, whereas LATTE consistently undershoots the gain from PIC simulations at the same frequencies. The state vector was again sampled at discrete positions along each TWT stage after being cascaded through transfer matrices and the sever like in the previous example. The power of the RF wave guided along the circuit is plotted vs distance at an operating frequency of 12 GHz, as shown in Fig. 12b. In



addition, the approximate RF power is plotted using data from electric field probes in PIC simulations, using the method discussed in the previous subsection. Plotting the RF power against the position-dependent attenuation profile of the SWS, we observe that the RF power increases up to about 70 mm from the input port, becomes extremely small at the sever gap, and then grows back with distance in the output stage of the TWT. Unlike the case of the single-stage TWT, the power of the state vector,  $P(z) = \frac{1}{2}\text{Re}(V(z)I^*(z))$ , for the two-stage TWT exhibits ripples along the length of the first stage with and without accounting for mismatches at the TWT ports; this is due to the reflections caused by the capacitive pi network of the sever shown in Fig. 10 that connects the two stages, as explained in Appendix D. Gain ripples have also been observed in TWTs with multiple reflections in [23]. As explained in the above subsection for the single-stage TWT, the apparent higher RF power at output port of the TWT when mismatches are present in Fig. 10 is due to our assertion that the accepted (i.e., input) RF power of the TWT is a constant  $-10$  dBm, while the available RF power at the input of the TWT is larger when there is an input impedance mismatch. Furthermore, for the case of  $-10$  dB mismatches at the TWT ports, a gain ripple of approximately 5 dB near the center frequency is present. The gain ripple is more significant for the two-stage TWT example shown due to the higher gain and additional reflections at the sever that are not completely attenuated. Gain ripple is generally undesirable for practical TWTs and can be mitigated in two ways: (a) by improving the match at the helix-to-coax or helix-to-waveguide transitions at the input and output port of the TWT with various geometries [36] or different dimensions, and (b) significantly increasing the attenuation leading into the sever gap region to further mitigate reflected waves.

## IX. COMPARISON TO LATTE

The TWT code LATTE requires the same frequency- and position-dependent inputs as our generalized Pierce model, which, aside from the electron beam parameters, are: interaction impedance, phase velocity, and the attenuation coefficient. However, LATTE differs from our model in that it is a Lagrangian-based model; it treats the electron beam as disks of charge, each interacting individually with the guided EM mode and other disks of charge [56]. Unlike our model, this feature allows LATTE to also simulate nonlinear effects such as intermodulation distortion, as well as large-signal TWT behavior. Many Eulerian- and Lagrangian-based TWT codes also exist which have been validated and studied in literature [57–65]. Furthermore, since the average voltage and current of the beam cannot vary in both the original and our generalized Pierce model, the beam cannot lose average

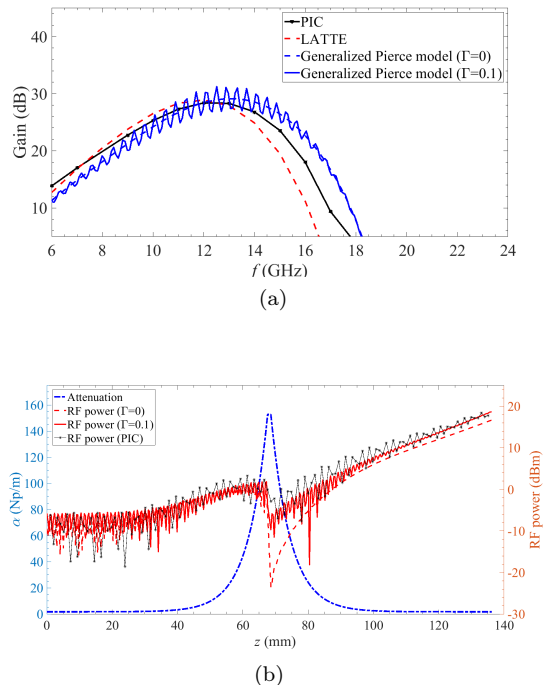


Figure 12: (a) Gain vs frequency for a two-stage TWT with no mismatches on both ports ( $\Gamma = 0$ , dashed blue line), and with a  $-10$  dB reflection on both ports ( $\Gamma = 0.1$ , solid blue line) calculated using model described in this paper and compared to PIC and LATTE simulations. (b) Plot of attenuation coefficient and calculated RF power along the SWS versus longitudinal position at 12 GHz with and without a  $-10$  dB mismatch (dashed red and solid red lines, respectively) at the TWT ports using our generalized Pierce model, in addition to the approximate RF power calculated from field monitors in PIC simulations (black line with dots).

power to the growing RF wave and net energy conservation is not possible in such a system. Due to this fact, our model is only useful in the small-signal regime. However, we also show a simple demonstration in Appendix H that, in the small-signal regime, the time-average power transfer per unit length between the beam and guided RF wave is nearly conserved under certain conditions.

However, in the small-signal regime, we believe that the way that LATTE models the sever gap in multi-stage TWTs is less accurate than our generalized Pierce model; LATTE ignores impedance mismatches at the sever gap and instead considers the sever gap as a continuous length of SWS. This approximation is valid only if the sever gap is negligibly small with respect to the guided wavelength and if there is sufficient attenuation to completely suppress reflections which occur at the sever gap. Furthermore, our transmission line-based model allows us to consider the effect of unavoidable mismatches at the



input/output terminations of the TWT, in addition to mismatches that may occur at the sever gap. The code LATTE does not have such capabilities at this time. In the best case, any mismatches that are present on the TWT will only lead to gain ripple. In the worse case, the TWT may become an oscillator. The ability to calculate the effect of such mismatches in our generalized Pierce model makes it possible to obtain hot two-port parameters (i.e., the parameters relating equivalent circuit voltages and currents at the output of the tube to the input of the tube) for complex TWT designs and, in a future work, predict the small-signal stability like is done for two-port microwave transistor amplifiers in Ref. [55, Ch. 3] (in terms of the parameters  $K$  and  $\Delta$ , there defined, which depend on active scattering parameters).

## X. CONCLUSION

We have showcased a method for determining the small-signal gain of spatially inhomogeneous, lossy, and dispersive single-stage and multi-stage TWTs using a generalized Pierce model. The results of our model were compared against the Lagrangian TWT code LATTE and against full-wave PIC simulations in CST, with a peak gain that agrees within 1 dB and within 0.6 GHz with full-wave PIC simulations (when considering matched terminations at both ends of the TWT). Furthermore, our Pierce-like model uses the helix dispersive characteristic impedance,  $Z_c$ , and a dispersive beam wave coupling factor,  $a$ , that depends on the interaction Pierce impedance,  $Z_p$ . The imperfect but realistic helix sever in our multi-stage TWT model is represented using a capacitive pi-network. Furthermore, since our model is based on equivalent TLTs and loads, we are able to consider how impedance mismatches at the input and output ports of the TWT lead to gain ripple.

Since our model allows for spatially inhomogeneous and dispersive TWT structures to be used, it may serve as a simple and useful tool for TWT designers to determine suitable and practical TWT lengths, loss patterns, or pitch profiles for desired small-signal behavior. From our four-port transfer matrices for both the single-stage and two-stage TWT models, it may also be possible to determine the “hot” two-port scattering parameters of the TWT and compute the corresponding small-signal stability factors. Knowledge of these hot scattering parameters may allow TWT designers to check for zero-drive stability in their TWT designs before performing time-consuming PIC simulations.

## ACKNOWLEDGMENTS

This material is based upon work supported by the Air Force Office of Scientific Research MURI award number FA9550-20-1-0409 administered through the University of New Mexico. The authors thank DS SIMULIA for

providing CST Studio Suite, which has been instrumental in this study.

## CONFLICT OF INTEREST

The authors have no conflicts to disclose.

## DATA AVAILABILITY

The data that support the findings of this study are available from the corresponding author upon reasonable request.

## Appendix A: Characteristic Impedance of Guided Modes in a Helix SWS

Following the work of [30, 31], we determine the characteristic impedance of modes guided by a realistic helix SWS by approximating the tape helix as a lossless, anisotropically conducting tube, called the sheath helix, which was derived in [66]. Using the sheath model, one may define the transmission line equations in terms of a voltage,  $V$ , defined as the potential difference between the surface of the sheath helix and the conducting wall which encloses the helix, and a current,  $I$ , which is defined as the longitudinal component of the current conducted by the sheath helix. The characteristic impedance of this sheath helix is also called the longitudinal characteristic impedance in [31, 36]. Paik also provides a transverse characteristic impedance definition in [31] which is proportional to the longitudinal impedance by the ratio of the group velocity to the phase velocity  $v_g/v_c$ , as explained in [31]. In this paper, we wish to use the longitudinal characteristic impedance definition, since the it satisfies the power equation for forward voltage and current waves  $P^+(z) = \frac{1}{2}Z_c |I^+(z)|^2$ , where the per-unit-length inductance and capacitance are calculated below as was done in [30, 31]. We will refer to the longitudinal characteristic impedance as “characteristic impedance” in the remainder of this appendix.

Using these definitions for voltage and current, the transmission line equations in the phasor domain (with implicit time dependence as  $e^{j\omega t}$ ) in terms of per-unit-length inductance and capacitance for a mode guided by a lossless uniform helix SWS are  $\frac{dV(z)}{dz} = -j\omega LI(z)$  and  $\frac{dI(z)}{dz} = -j\omega CV(z)$ , where the per-unit-length frequency-dependent inductance  $L$  and capacitance  $C$  equations for case 5 in [31] are shown below. Using the derivation from [31], the characteristic impedance of the lossless sheath helix may be determined numerically at each frequency as

$$Z_c = \frac{v_c}{v_g} \sqrt{\frac{L}{C}}. \quad (\text{A1})$$

To compute the characteristic impedance we must compute the quantities  $L$  and  $C$  which are given by

$$L = L_0 [1 - \kappa_1^2(\gamma r_h, \gamma r_w)] \quad (\text{A2})$$

and

$$C = C_0 [1 + (\theta N_r / (2\pi)) (\epsilon_r - 1) D(\gamma r_h)] [1 - \kappa_c^2(\gamma r_h, \gamma r_w)]^{-1} \quad (\text{A3})$$

where  $L_0 = \mu_0 \beta_c^2 / (2\pi \gamma^2) \cot^2 \Psi [I_1(\gamma r_h) K_1(\gamma r_h)]$  and  $C_0 = 2\pi \epsilon_0 / [I_0(\gamma r_h) K_0(\gamma r_h)]$  are the per-unit-length inductance and capacitance of a sheath helix of pitch angle  $\Psi = \tan^{-1} [d / (2\pi r_h)]$  in free space,  $I_1$  and  $K_1$  are modified Bessel functions of order 1,  $I_0$  and  $K_0$  are modified Bessel functions of order 0. Furthermore, the quantities  $[1 - \kappa_1^2(\gamma r_h, \gamma r_w)]$  and  $[1 - \kappa_c^2(\gamma r_h, \gamma r_w)]^{-1}$  in Eqns. (A2) and (A3) are the correction factors that account for the metal walls enclosing the helix, with  $\kappa_1^2(\gamma r_h, \gamma r_w) = [I_1(\gamma r_h) K_1(\gamma r_w)] / [I_1(\gamma r_w) K_1(\gamma r_h)]$  and  $\kappa_c^2(\gamma r_h, \gamma r_w) = [I_0(\gamma r_h) K_0(\gamma r_w)] / [I_0(\gamma r_w) K_0(\gamma r_h)]$ . The factor  $[1 + (\theta N_r / (2\pi)) (\epsilon_r - 1) D(\gamma r_h)]$  in Eqn. (A3) accounts for the dielectric loading of  $N_r = 3$  rods that have relative permittivity  $\epsilon_r$  that subtend an angle  $\theta$ , where  $D(\gamma r_h) = (\gamma r_h) I_0(\gamma r_h) K_1(\gamma r_h)$ .

The equations (A2) and (A3) are substituted into the dispersion relation

$$\beta_c = \omega \sqrt{LC}, \quad (\text{A4})$$

to solve for the longitudinal propagation constant  $\beta_c$  and angular frequency  $\omega$  in terms of the radial propagation constant,  $\gamma^2 = \beta_c^2 - k_0^2$ , where  $k_0 = \omega \sqrt{\mu_0 \epsilon_0}$ . Once the relation between the propagation constant and angular frequency are numerically calculated from Eqn. (A4), the per-unit-length inductance and capacitance of Eqns. (A2) and (A3), respectively, can be calculated, along with the characteristic impedance in Eqn. (A1) that we wish to find.

Interestingly, we find that the cold phase velocity ( $v_c = \omega / \beta_c$ ) calculated from the dispersion relation in Eqn. (A4) gives a reasonable approximation of the phase velocities for the real tape helix structure, as demonstrated in Fig. 4, determined from full-wave eigenmode simulations in CST Studio Suite, even though it approximates the helix using the sheath model.

## Appendix B: Alternative State Vector and System Matrix

As explained in the body of this paper and in Sec. A, the choice of voltage, current, and characteristic impedance definitions for a forward mode guided

along the helix must satisfy the power relation  $P = \frac{1}{2} \text{Re}[V^+ I^{+*}]$ , where in the cold TL (i.e., without dependent current generator) one has  $Z_c = V^+ / I^+$ . Knowledge of this characteristic impedance is useful in the design of well-matched input or output ports on the TWT. However, in the original Pierce model, the characteristic impedance of the effective transmission line is the interaction impedance,  $Z_P$  [2, 3, 21]. These two impedances are related in this paper by the coupling coefficient  $a$  at each frequency. This coupling coefficient has also been used in other works such as [20, 25–27, 67–74].

As derived in the appendix of [22], the interaction impedance and characteristic impedance of the cold SWS are related through the frequency-dependent coupling coefficient  $a$ , as

$$a^2 = \frac{Z_P}{Z_c}. \quad (\text{B1})$$

Using this relation between the helix characteristic impedance and interaction impedance, one can transform the transmission line voltage and current of the state vector in Eqn. (1) and system matrix in Eqn. (2) to be in terms of scaled TL quantities  $V'(z) = aV(z)$  and  $I'(z) = I(z)/a$  that maintain the average power definition  $P = \frac{1}{2} \text{Re}[V(z)I(z)^*] = \frac{1}{2} \text{Re}[V'(z)I'(z)^*]$ , where  $a$  is the same coupling coefficient that relates interaction impedance to characteristic impedance. Looking at transformed forward propagating wave, the TL characteristic impedance is the same as the interaction (or Pierce) impedance, i.e.,  $V^+ / I^+ = Z_P$ . By making this transformation, the state vector and system matrix are represented (with transmission line segment subscript  $s$  suppressed) as

$$\partial_z \Psi'(z) = j \underline{\mathbf{M}}' \Psi'(z), \quad (\text{B2})$$

where the transformed state vector is

$$\Psi'(z) = \left[ V'(z), I'(z), V_b(z), I_b(z) \right]^T, \quad (\text{B3})$$

and the transformed system matrix may be expressed in terms of interaction impedance rather than characteristic impedance as  $Z_P = a^2 Z_c$ .

$$\underline{\mathbf{M}}' = \begin{bmatrix} 0 & k_c Z_P & 0 & 0 \\ k_c / Z_P & 0 & -g & -\beta_0 \\ 0 & k_c Z_P & \beta_0 & \zeta_{sc} \\ 0 & 0 & g & \beta_0 \end{bmatrix}. \quad (\text{B4})$$

We find that, with this transformation, the coupling coefficient is suppressed from the matrix and one can use  $Z_P$  as the characteristic impedance with the transformed TL parameters  $V'$  and  $I'$ . This alternate formulation for the system matrix is useful, since the interaction impedance can be readily found for a realistic helix SWS

using full-wave eigenmode simulations and postprocessing as in Eqn. (5), whereas it may be difficult to define and determine the equivalent voltage and current and the associated characteristic impedance in a realistic tape helix SWS. Furthermore, this alternate system matrix formulation more closely matches the original works by Pierce [2, 3, 21]. The transformed system matrix  $\underline{\mathbf{M}}'$  may be used in place of the system matrix  $\underline{\mathbf{M}}$  shown in Eqn. (2) for segments of homogeneous transmission lines. Furthermore, the power gain and “hot” modal dispersion diagram (for homogeneous structures) of TWTs modeled using the transformed system matrix  $\underline{\mathbf{M}}'$  will be the same as those found using the original system matrix  $\underline{\mathbf{M}}$ , based on the fact that  $P = \frac{1}{2}\text{Re}[V(z)I(z)^*] = \frac{1}{2}\text{Re}[V'(z)I'(z)^*]$ . The only thing that differs in using  $\Psi(z)$  or  $\Psi'(z)$  is that the *matching terminations* applied to the input and output of the SWS are either  $Z_c$  or  $Z_P$ , respectively. This does not mean that the TWT ports should be terminated in reality using one impedance or the other, it means that the definition of characteristic impedance of the equivalent transmission line and source and load impedances must be consistent with the chosen voltage and current definitions. For helix-based SWSs, the source and load impedances  $Z_S$  and  $Z_L$  that match the SWS’ actual characteristic impedance are close to  $Z_c$  (using the sheath helix model to analytically approximate the characteristic impedance and modal dispersion of a tape helix, see Appendix A). When using the transformed TL parameters  $V'$  and  $I'$ , the definition of impedance changes by a factor  $a^2$  and, in this new basis, the transformed source and load impedances are  $a^2Z_S$  and  $a^2Z_L$ , that match with the characteristic impedance  $Z_P$  of the SWS. The method described in this paper can be used also for unmatched loads, with the mismatch properly taken into account via the boundary conditions in Eqns. (15) or (16) for the single-stage or two-stage TWT, respectively, as shown in Sec. VIII.

We note that in the body of this paper, we used the notation with  $V$  and  $I$  described in Sec. III, and the associated frequency-dependent characteristic impedance  $Z_c$  for the helix SWS. We also evaluated the frequency-dependent interaction impedance  $Z_P$  using results from the eigenmode solver of CST Microwave Studio, as described in Sec. V and shown in Fig. 4. Using the calculated, frequency-dependent, characteristic impedance  $Z_c$  and the frequency-dependent interaction impedance  $Z_P$  from full-wave eigenmode simulations, we determined the frequency-dependent coupling coefficient  $a$  through the relation in Eqn. B1.

### Appendix C: Attenuation Pattern

For a single-stage helix TWT, adiabatic position-dependent loss patterning is added to the dielectric support rods (via carbon coating) to attenuate any reflected waves that can occur due to imperfect matching at the input and output ports of the TWT. Thus, we represent

this loss patterning in full-wave PIC simulations by scaling the bulk loss tangent of the dielectric rods at each position along the structure, with the same position-dependent profile as our desired attenuation coefficient used in our theoretical model. In a single-stage TWT, this attenuation pattern is typically Gaussian in shape, with a peak attenuation halfway between the input and output ports, as shown in Fig. 11b. This Gaussian profile is defined (in Np/m) as

$$\alpha_c(z) = \Delta_\alpha e^{-(z-l/2)^2/(2\sigma^2)} + \alpha_{\min}, \quad (\text{C1})$$

where  $\Delta_\alpha = \alpha_{\max} - \alpha_{\min}$ ,  $\alpha_{\max}$  is the peak attenuation coefficient in the center of the SWS corresponding to the region where the loss tangent of the dielectric support rods is at its maximum,  $\alpha_{\min}$  is the attenuation coefficient at the input or output ends of the SWS where the loss tangent of the dielectric rods is at its minimum,  $l$  is the total length of the single-stage SWS,  $\sigma = l_\alpha / \left(2[2\ln(2)]^{1/2}\right)$ , and  $l_\alpha$  (effective loss length) is the FWHM of the Gaussian profile.

Severs are typically implemented in multi-stage helix TWTs by creating a physical gap between stages, where both helices at the gap are left unterminated or short-circuited to the barrel of the TWT. Near the sever, adiabatic, position-dependent loss patterning is again added to the dielectric support rods to strongly attenuate reflected waves at the open/short circuited ends of the sever in the same manner described for single-stage TWTs. In multi-stage TWTs, this loss patterning is typically exponential in shape leading to either end of the sever, as shown in Fig. 12b. We represent the position-dependent attenuation coefficient (in Np/m) as an exponential decaying function from each end of the sever towards the input/output port with a piecewise function as

$$\alpha_c(z) = \begin{cases} \Delta_\alpha e^{(z-l_1)\frac{5}{l_\alpha}} + \alpha_{\min} & 0 \leq z < l_1 \\ \Delta_\alpha e^{-(z-l_{1+g})\frac{5}{l_\alpha}} + \alpha_{\min} & l_{1+g} \leq z < l_{\text{tot}} \\ 0 & l_1 \leq z < l_{1+g} \end{cases} \quad (\text{C2})$$

where for the two-stage TWT,  $l_\alpha$  is the effective length of the attenuation pattern on each stage, the distance at which the attenuation decays to approximately 99% from its peak value. Furthermore,  $l_1$  and  $l_2$  are the lengths of the first and second stages of the TWT, respectively,  $l_{1+g} = l_1 + l_{\text{gap}}$ ,  $l_{\text{gap}}$  is the length of the sever gap between TWT stages, and  $l_{\text{tot}} = l_1 + l_{\text{gap}} + l_2$  is the total length of the SWS in a two-stage TWT. Between the two circuit stages, in the sever gap, there is only vacuum.

One can observe from Fig. 13a that the frequency-dependence of  $\alpha_{\min}$  can be fitted to a first-order polynomial  $\alpha_{\min} \approx 0.1035f_{\text{GHz}} + 0.1961$  Np/m and that the average value of  $\alpha_{\max}/\alpha_{\min}$  is approximately 80 over the band of interest. Although the ratio  $\alpha_{\max}/\alpha_{\min}$  varies by as much as  $\pm 6\%$  from the average value, this frequency-dependence does not make a notable difference in the

gain-vs-frequency plots. Using a maximum attenuation coefficient of  $\alpha_{\max} = 84.8\alpha_{\min}$  or  $\alpha_{\max} = 75.2\alpha_{\min}$  (i.e.  $\pm 6\%$  deviation from the average scaling factor of 80) did not alter the shape of gain-vs-frequency profiles of our model or LATTE with respect to PIC results, only their peak gain. Thus, for simplicity, we use a constant scaling factor of  $\alpha_{\max} = 80\alpha_{\min}$  in our model. By scaling  $\alpha_{\min}$  to obtain  $\alpha_{\max}$ , we make the simplifying assumption that attenuation coefficients in the low-loss and high-loss regions of the SWS have the same dependence on frequency. For the frequency range of interest, this appears to be a reasonable approximation. Additionally, we do not consider how large losses affect the phase velocity and interaction impedance of the cold structure in our above examples.

In Fig. 13b we show the attenuation coefficient versus dielectric loss tangent, where the dielectric loss tangent is related to the minimum loss tangent by the scaling factor,  $\tau$ , as  $\tan \delta = \tau \tan \delta_{\min}$ . It is clear that the attenuation coefficient is related to the loss tangent of our dielectric support rods by a first order polynomial  $\alpha \approx 0.05825\tau + 1.406$  Np/m. In Fig. 13b, the vertical offset of the attenuation coefficient when there is no dielectric loss tangent is due to metal losses in the copper walls and tungsten helix. The first-order relationship between the dielectric loss tangent and attenuation coefficient is useful because the position-dependent attenuation profile will have an identical shape to the position-dependent loss tangent profile that we impose in full-wave PIC simulations.

#### Appendix D: Sever Gap Transfer Matrix

An imperfect sever, i.e. one that allows EM waves to weakly transmit between stages separated by a gap, can be represented as a capacitive pi network in the helix structure. This is similar to the classical case of a discontinuity in the center conductor of a coaxial transmission line [51–53], except the center conductor is hollow and helical in shape for our case. Due to this difference, it is necessary to simulate the sever gap in a full-wave solver to approximate the gap capacitance. However, it becomes necessary to simplify the geometry even further to excite the proper modes and accurately compute the gap capacitance. In our simplified full-wave model for the sever gap, we replace the center helix with a hollow inner conductor of the same inner and outer radii, as shown in Fig. 14. This simplified model allows TEM waves to be excited by both wave ports to the left and right of the sever gap. The wave ports are both positioned 5 mm away from the ends of the 1 mm sever gap, with reference planes on each side of the inner conductor discontinuity. The disagreement between our PIC results and our model for the two-stage TWT in Sec. VIII may partially be attributed to this simplified model for the sever gap. A more complex model (with a tape helix in-

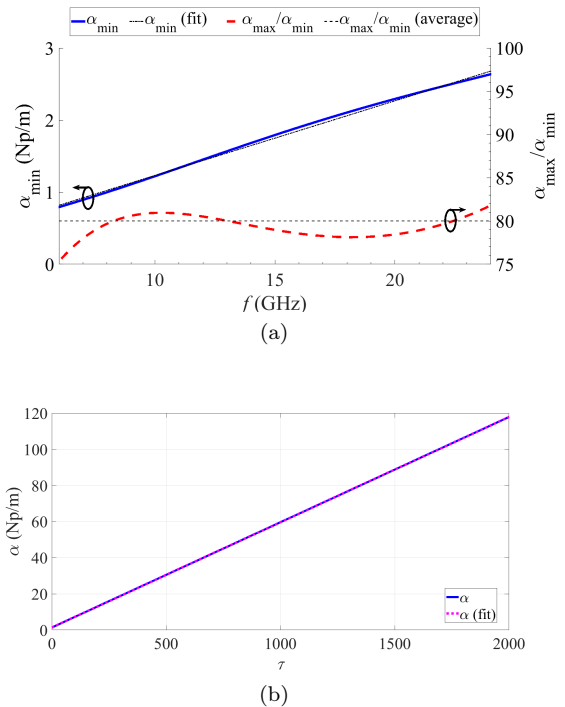


Figure 13: (a) Attenuation coefficient,  $\alpha_{\min}$ , and ratio of maximum attenuation coefficient to minimum attenuation coefficient versus frequency for the helix SWS. The minimum attenuation coefficient corresponds to the region of the SWS with dielectric rods without loss coating, i.e., the attenuation at the input or output ports of the TWT labeled in Fig. 1, (b) Attenuation coefficient versus dielectric loss tangent scaling factor at 12 GHz. Attenuation is due to the lossy dielectric rods, tungsten helix, and copper outer wall. The attenuation coefficient for the SWS is related to the frequency by a first-order polynomial fitting (dotted black lines), as is the relationship between the loss tangent scaling factor and attenuation coefficient (magenta dashed line).

stead of a hollow tube for the center conductor) can be used in future works to accurately model the sever gap, however it will be a significant challenge to excite the proper helix modes and find the scattering parameters at the reference planes of the gap.

Using full-wave simulations, we compute the scattering parameters of the simplified two-port sever gap network and convert them to ABCD parameters by using the helix characteristic impedance from Appendix A. The equivalent frequency-dependent series and shunt capacitances of the sever gap can then be calculated from the forward ABCD parameters [32, (Ch. 4)] as

$$\begin{cases} C_1 = \frac{-1}{j\omega B} \\ C_2 = AC_1 - C_1 \end{cases} \quad (\text{D1})$$

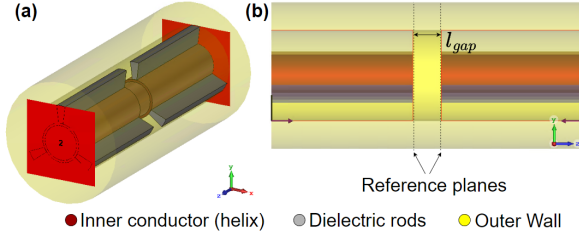


Figure 14: Model for determining equivalent capacitive pi network of a helix sever gap. (a) Isometric view of CST model, and (b) side view of CST model.

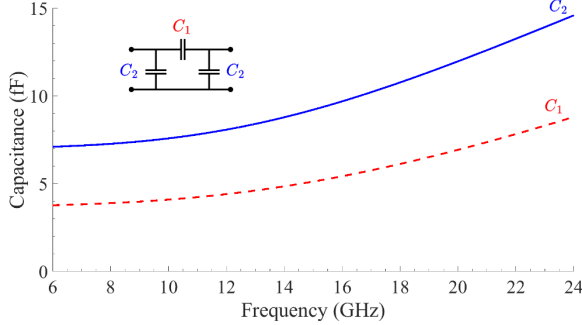


Figure 15: Equivalent two-port pi-network of helix sever gap and the corresponding capacitance values versus frequency.

Conversely, the two-port ABCD parameters of the capacitive pi network shown in Fig. 15 can be represented as

$$\begin{bmatrix} V_2 \\ I_2 \end{bmatrix} = \mathbf{T}_{\text{gap},c} \begin{bmatrix} V_1 \\ I_1 \end{bmatrix}, \quad (\text{D2})$$

where

$$\mathbf{T}_{\text{gap},c} = \begin{bmatrix} \frac{C_1+C_2}{C_1} & \frac{-1}{j\omega C_1} \\ -j\omega(2C_1C_2+C_2^2) & \frac{C_1+C_2}{C_1} \end{bmatrix}. \quad (\text{D3})$$

### Appendix E: Plasma Frequency Reduction Factor

For an electron beam moving at an average velocity  $u_0$ , these plasma frequency oscillations result in propagating fast and slow space charge waves (relative to the average electron velocity). The plasma frequency of a linear electron beam of cross-sectional area,  $A$ , is given as,

$$\omega_p = \sqrt{-\frac{\rho_0 \eta}{A \epsilon_0}} = \sqrt{\frac{I_0 u_0}{2V_0 A \epsilon_0}}. \quad (\text{E1})$$

As explained in [75–77], the finite cross-section of the electron beam, along with surrounding metallic walls will

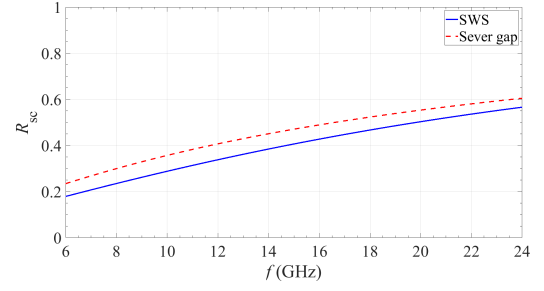


Figure 16: Plasma frequency reduction factor versus frequency in the SWS and in the sever gap regions

make the scalar electric potential of the electron beam nonuniform over the beam cross-section. Because of this fact, the plasma frequency of the beam will be reduced by a plasma frequency reduction factor ( $R_{sc}$ ),  $\omega_q = R_{sc}\omega_p$ . The closed-form frequency-dependent value we use for  $R_{sc}$  is calculated from [76, 78] as,

$$R_{sc}^2 = 1 - 2I_1(\beta_0 r_b) \left( K_1(\beta_0 r_b) + \frac{K_0(\beta_0 r_h)}{I_0(\beta_0 r_h)} I_1(\beta_0 r_b) \right), \quad (\text{E2})$$

where, we assume the beam has a cylindrical cross-section with radius  $r_b$  and the helix is approximated as a metallic cylinder with inner radius  $r_h$ . Furthermore,  $I$  and  $K$  are modified Bessel functions of the first and second kind, respectively. A formulation for  $R_{sc}$  for the case of an electron beam confined by a helical slow-wave structure, which is approximated using the sheath helix model, has also been provided in [78], though it is not as trivial to use. In the sever gap region of the multi-stage TWT, we calculate  $R_{sc}$  from Eqn. (E2) like above, but with the wall radius  $r_w$  substituted in place of  $r_h$ . The reduction factor in both the SWS and the sever gap region is plotted versus frequency in Fig. 16.

### Appendix F: Hot Dispersion Relation from System Matrix in a Uniform TWT

In the supplementary material of [20], it was shown that the modal solutions for a hot TWT in the form  $\Psi(z) = \Psi e^{-jkz}$  can be found from the dispersion equation  $\text{Det}(\mathbf{M} - k\mathbf{I}) = 0$  that matches the fourth-order dispersion relation from Pierce theory [21, Ch. 2] [37, Ch. 8], where  $\mathbf{I}$  is a  $4 \times 4$  identity matrix and  $k$  is the hot complex propagation constant of the TWT system. Like in [20], the dispersion relation for a lossy TWT is calculated from the determinant of the system matrix in Eqn. (2) to demonstrate that it is the same as the one found in conventional Pierce theory [21, Ch. 2] [37, Ch. 8].

The fourth-order dispersion equation for the lossy TWT is found from the determinantal equation above as



$$(k^2 - k_c^2) \left( (k - \beta_0)^2 - \zeta_{sc} g \right) = -a^2 g Z_c k_c k^2 \quad (\text{F1})$$

where  $k_c$  has complex value and  $Z_c$  is assumed to be real under the low-loss approximation discussed in Sec. III. The Pierce gain parameter is defined as  $C^3 = a^2 Z_c I_0 / (4V_0)$  (where the term  $a^2 Z_c$  has been substituted for  $Z_P$ ) and the plasma propagation constant is defined as  $\beta_q = \omega_q / u_0$ . Substituting the Pierce gain parameter and plasma propagation constant into (F1), we obtain the conventional Pierce dispersion relation

$$(k^2 - k_c^2) \left( (k - \beta_0)^2 - \beta_q^2 \right) = -2C^3 k_c \beta_0 k^2. \quad (\text{F2})$$

If there are no losses (i.e.  $k_c = \beta_c$ ), the dispersion relation in Eqns. (F1) and (F2) match those found in the supplementary material of [20]. Furthermore, if one assumes that  $k \approx k_c$  like was done by Pierce, then  $k^2 - k_c^2 \approx 2k_c(k - k_c)$  and the fourth-order modal dispersion relation in Eqn. (F2) is reduced to a third-order dispersion relation which neglects the backward-propagating wave supported by the TWT and only considers three forward-propagating waves [21, Ch. 2][37, Ch. 8]

$$(k - k_c) \left( (k - \beta_0)^2 - \beta_q^2 \right) = -C^3 k_c^2 \beta_0. \quad (\text{F3})$$

This modal dispersion relation in Eqn. (F3) above is often used in conventional Pierce theory. A comparison between our generalized Pierce model (with considers all four waves in the TWT) and the conventional Pierce model (which considers only three waves) is shown for a homogeneous TWT example in Appendix G.

### Appendix G: Spatially Homogeneous TWT Example

To further validate our model, we provide a comparison between our model and the conventional three-wave model provided by Pierce [2, 3, 21, Ch. 9][37, Ch. 8], in terms of (i) the gain vs frequency, and (ii) RF power vs longitudinal distance, for the restrictive case of a simple, spatially homogeneous, dispersive, and lossy, single-stage TWT. The conventional Pierce model considers only three propagating hot waves in the TWT system and it neglects the backward wave supported by the TWT, whereas our model considers all four hot waves. The power gain of the conventional Pierce model is calculated as  $G_{\text{dB}}(z) = 20 \log_{10} |E(z)/E_0|$ , where the position-dependent longitudinal electric field along the TWT from [3, Eqn. 3.8] is  $E(z) = \frac{1}{3} E_0 e^{-j\beta_0 z} (e^{\delta_1 z} + e^{\delta_2 z} + e^{\delta_3 z})$ ,  $E_0$  is the longitudinal electric field at the start of the TWT, and the incremental propagation constant for each wave (subscripts 1, 2, 3) is  $\delta = -j(k - \beta_0) / (\beta_0 C)$ , which is determined from the three  $e$  wavenumber solutions

$k = k_1, k_2, k_3$ , respectively, that are calculated from the third-order dispersion relation shown in Eqn. (F3). With conventional Pierce theory, the gain of a finite-length TWT of length  $L$  is simply  $G_{\text{dB}}(L)$ .

In this example, the beam parameters, TWT length  $L$ , SWS dimensions, and input RF power are the same as described for the single-stage TWT example that was shown in Sec. VIII, with the difference that in this appendix only the intrinsic attenuation coefficient (i.e. the one associated to  $\alpha_{\text{min}}$ ) is used over the length of the TWT, which is frequency dependent but not position dependent, in both the conventional three-wave Pierce theory and our model (referred to as the generalized Pierce model in this paper). Furthermore, in both models, we consider the same dispersive parameters described in this work (such as wavenumber, attenuation coefficient, reduced plasma frequency, interaction impedance, characteristic impedance, and coupling coefficient  $a$ ).

We note that, unlike our generalized Pierce model, the conventional three-wave Pierce model that we use for comparison does not include a coupling parameter and instead assumes the characteristic impedance of the SWS to be equal to the interaction impedance  $Z_P$  (hence it assumes  $a = 1$ ), and both ends of the TWT are terminated with  $Z_P$ . In our model, the single-stage TWT is terminated on both ends with its cold characteristic impedance  $Z_c$  and its gain vs frequency is plotted in Fig. 17. Since there is no significant loss patterning in the center of the single-stage TWT as there was in the example in Sec. VIII, the peak gain is approximately 16 dB higher than the one found in Fig. 11a. Furthermore, the peak gain calculated from the conventional Pierce model is approximately 1.5 dB higher than the gain obtained from our generalized Pierce model that considers all four waves.

The RF power from our generalized Pierce model,  $P(z) = \frac{1}{2} \text{Re} [V(z)I(z)^*]$  obtained by using  $V(z)$  and  $I(z)$  of the state vector, is plotted against position for this spatially homogeneous example in Fig. 18. Whereas, for the conventional three-wave Pierce model, the position-dependent power is calculated from the position-dependent power gain as  $P(z) = P_{\text{in,dBm}} + G_{\text{dB}}(z)$  and is also plotted in Fig. 18, where the input power for both cases is  $P_{\text{in,dBm}} = -10$  dBm. The RF power at the collector-end of the TWT calculated from conventional Pierce theory is approximately 1 dBm higher than the power calculated by our model at 12 GHz.

### Appendix H: beam-wave power conservation

Referring to the homogeneous small-signal TL model shown in Fig. 2(b), using simple TL theory or Lagrangian theory, it is easy to show that the time-average power flowing in the TL is  $P_{\text{TL}} = \frac{1}{2} \text{Re} (VI^*)$ . In a lossless TL, the power variation  $dP_{\text{TL}}/dz$  is equal to the power transfer per-unit-length from the dependent current generator  $i_s = -a(dI_b/dz)$  (representing the effect of elec-

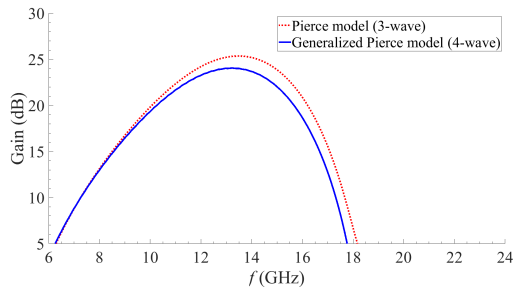


Figure 17: Gain vs frequency for a spatially homogeneous single-stage TWT using the generalized Pierce model discussed in this paper (solid blue), compared to that from Pierce’s conventional three-wave model (dotted red).

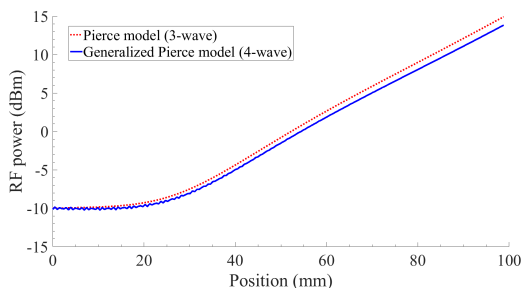


Figure 18: RF power vs position at 12 GHz for a spatially homogeneous single-stage TWT, calculated using our generalized Pierce model (solid blue), and Pierce’s conventional three-wave model (dotted red).

tron beam to the guided RF wave) [79, p. 309][27, p. 286][26], i.e.,

$$\frac{dP_{\text{TL}}}{dz} = \frac{1}{2} \text{Re}(Vi_s^*) = -\frac{1}{2} |V|^2 \text{Re}(Y_b^*), \quad (\text{H1})$$

where  $*$  denotes complex conjugation, and we have used the concept of electronic beam admittance per unit length  $Y_b = -i_s/V$  given in [22, 26]. In lossy TLs, there is an additional term that represents the attenuation along the TL. The time-average power transfer per-unit-length of TWT from the electron beam (considered as an impressed ac current source  $I_b$ ) to the guided RF wave, from [42, p. 359][37, p. 324][27, p. 168], is

$$\frac{dP_b}{dz} = \frac{1}{2} \text{Re}(E_z I_b^*), \quad (\text{H2})$$

where the axial electric field of the guided RF wave that couples to the electron beam is  $E_z = -a(dV/dz)$ . Considering the propagation constant  $k$  of the hot amplifying mode, we obtain the expressions  $E_z = jakV$  and  $I_b = ji_s/(ka)$ . Substituting these expressions for  $E_z$  and  $I_b$  into Eqn. (H2), we obtain

$$\frac{dP_b}{dz} = \frac{1}{2} \text{Re} \left( Vi_s^* \frac{ka}{(ka)^*} \right) = -\frac{1}{2} |V|^2 \text{Re} \left( Y_b^* \frac{ka}{(ka)^*} \right). \quad (\text{H3})$$

When the beam-wave coupling coefficient  $a$  is real (as considered in this paper) and  $|\text{Re}(k)| \gg |\text{Im}(k)|$ , the time-average powers per unit length are nearly equal, i.e.,  $dP_{\text{TL}}/dz \approx dP_b/dz$ . There is a slight inconsistency in the power of the guided RF wave calculated using Eqn. (H3), compared to Eqn. (H1). However, the inconsistency between powers is negligible in the small-signal regime, since  $\text{Re}(k)$  is typically one to two orders of magnitude larger than  $\text{Im}(k)$ , as demonstrated in [20, 22, 80]. This inconsistency in calculated powers is intrinsic to the Pierce model that we base our model upon [2, 3, 21] (the Pierce model assumes that  $a = 1$ ). However, it has been demonstrated in [27, Ch. 22][81] that the Pierce model remains energetically self-consistent from the Lagrangian point of view.

- 
- [1] C. K. Chong and W. L. Menninger, IEEE Transactions on Plasma Science **38**, 1227 (2010).
- [2] J. Pierce, Proceedings of the IRE **35**, 111 (1947).
- [3] J. Pierce, Bell System Technical Journal **30**, 626 (1951).
- [4] C. Paoloni, D. Gamzina, R. Letizia, Y. Zheng, and N. C. Luhmann Jr, Journal of Electromagnetic Waves and Applications **35**, 567 (2021).
- [5] M. Bodmer, J. Laico, E. Olsen, and A. Ross, Bell System Technical Journal **42**, 1703 (1963).
- [6] A. Jacquez and G. Wada, in *1986 International Electron Devices Meeting* (IEEE, 1986) pp. 501–504.
- [7] O. Sauseng, J. M. Johnston, and C. M. Leigh, in *IEEE Digest on Aerospace Applications Conference* (IEEE, 1988) pp. 6–1.
- [8] V. Srivastava, T. Ghosh, M. Akhtar, and S. Joshi, IETE Technical review **16**, 249 (1999).
- [9] J. D. Wilson, P. Ramins, D. A. Force, H. C. Limburg, and I. Tammaru, in *International Electron Devices Meeting 1991 [Technical Digest]* (IEEE, 1991) pp. 585–588.
- [10] S. K. Datta, V. B. Naidu, S. U. Reddy, L. Kumar, and B. N. Basu, IEEE transactions on plasma science **37**, 311 (2009).
- [11] M. A. Frisoni, *Theoretical design study of a 2-18 GHz bandwidth helix TWT amplifier* (Rome Air Development Center, Air Force Systems Command, 1987).
- [12] B. Braatz, G. Dohler, and G. Groshart, in *1987 International Electron Devices Meeting* (IEEE, 1987) pp. 466–469.
- [13] A. Gilmour, in *Principles of traveling wave tubes* (Norwood, MA, USA: Artech House, 1994) Chap. 12, pp. 323–357.
- [14] A. Gilmour, *Principles of traveling wave tubes* (Norwood, MA, USA: Artech House, 1994).
- [15] V. Srivastava, R. G. Carter, B. Ravinder, A. Sinha, and S. Joshi, IEEE Transactions on Electron Devices **47**, 2438 (2000).

- [16] T. K. Ghosh, A. J. Challis, A. Jacob, D. Bowler, and R. G. Carter, *IEEE transactions on electron devices* **55**, 668 (2008).
- [17] T. K. Ghosh, A. J. Challis, A. Jacob, and D. Bowler, *IEEE Transactions on Electron Devices* **56**, 1135 (2009).
- [18] M. K. Alaria, A. Bera, R. Sharma, and V. Srivastava, *IEEE Transactions on Plasma Science* **39**, 550 (2010).
- [19] S.-S. Jung, A. V. Soukhov, B. Jia, and G.-S. Park, *Applied physics letters* **80**, 3000 (2002).
- [20] K. Rouhi, R. Marosi, T. Mealy, A. F. Abdelshafy, A. Figotin, and F. Capolino, *Applied Physics Letters* **118**, 263506 (2021).
- [21] J. R. Pierce, *The bell System technical journal* **29**, 1 (1950).
- [22] K. Rouhi, R. Marosi, T. Mealy, A. Figotin, and F. Capolino, *IEEE Transactions on Plasma Science* (2024).
- [23] D. Chernin, I. Rittersdorf, Y. Lau, T. M. Antonsen, and B. Levush, *IEEE transactions on electron devices* **59**, 1542 (2012).
- [24] A. Jassem, Y. Lau, D. P. Chernin, and P. Y. Wong, *IEEE Transactions on Plasma Science* **48**, 665 (2020).
- [25] A. Figotin and G. Reyes, *Journal of Mathematical Physics* **54**, 111901 (2013).
- [26] V. A. Tamma and F. Capolino, *IEEE Transactions on Plasma Science* **42**, 899 (2014).
- [27] A. Figotin, *An Analytic Theory of Multi-stream Electron Beams in Traveling Wave Tubes* (World Scientific, 2021).
- [28] N. Marcuvitz and J. Schwinger, *Journal of Applied Physics* **22**, 806 (1951).
- [29] L. B. Felsen and N. Marcuvitz, *Radiation and scattering of waves*, Vol. 31 (John Wiley & Sons, 1994).
- [30] G. Kino and S. Paik, *Journal of Applied Physics* **33**, 3002 (1962).
- [31] S. Paik, *IEEE Transactions on Electron Devices* **16**, 1010 (1969).
- [32] D. M. Pozar, *Microwave engineering* (John Wiley & Sons, NJ, USA, 2009).
- [33] R. E. Collin, *Field theory of guided waves* (McGraw-Hill, 1960).
- [34] S. Ramo, J. R. Whinnery, and T. Van Duzer, *Fields and waves in communication electronics* (John Wiley & Sons, 1994).
- [35] T. Mealy, A. F. Abdelshafy, and F. Capolino, *Physical Review Applied* **14**, 014078 (2020).
- [36] W. J. Henningsen, *Coupling transitions for travelling wave tubes.*, Ph.D. thesis, US Naval Postgraduate School, Monterey, California (1955).
- [37] S. E. Tsimring, *Electron beams and microwave vacuum electronics* (John Wiley & Sons, 2006).
- [38] W. C. Daywitt, *IEEE transactions on instrumentation and measurement* , 98 (1985).
- [39] C. L. Kory and J. A. Dayton, *IEEE Transactions on Electron Devices* **45**, 966 (1998).
- [40] C. L. Kory and J. A. Dayton, *IEEE Transactions on Electron Devices* **45**, 972 (1998).
- [41] M. Aloisio and P. Waller, *IEEE Transactions on Electron Devices* **52**, 749 (2005).
- [42] J. W. Gewartowski and H. A. Watson, *Principles of electron tubes: including grid-controlled tubes, microwave tubes, and gas tubes* (Van Nostrand, 1965).
- [43] A. K. MM, S. Aditya, and C. Chua, *IEEE Transactions on Electron Devices* **64**, 1868 (2017).
- [44] A. B. de Alleluia, A. F. Abdelshafy, P. Ragulis, A. Kuskov, D. Andreev, M. A. Othman, B. Martinez-Hernandez, E. Schamiloglu, A. Figotin, and F. Capolino, *IEEE Transactions on Plasma Science* **48**, 4356 (2020).
- [45] R. Marosi, T. Mealy, A. Figotin, and F. Capolino, *IEEE Transactions on Plasma Science* **50**, 4820 (2022).
- [46] P. R. R. Rao, V. A. Deshmukh, S. K. Datta, and L. Kumar, *AEU-International Journal of Electronics and Communications* **64**, 280 (2010).
- [47] V. B. Naidu, S. K. Datta, P. R. R. Rao, A. K. Agrawal, S. U. Reddy, L. Kumar, and B. Basu, *IEEE transactions on electron devices* **56**, 945 (2009).
- [48] V. Kumar, A. Vohra, and V. Srivastava, *New Carbon Materials* **23**, 378 (2008).
- [49] D. M. Goebel, J. G. Keller, W. L. Menninger, and S. T. Blunk, *IEEE Transactions on Electron Devices* **46**, 2235 (1999).
- [50] D. M. Goebel, *IEEE Transactions on Electron Devices* **47**, 1286 (2000).
- [51] J. Whinnery, H. Jamieson, and T. E. Robbins, *Proceedings of the IRE* **32**, 695 (1944).
- [52] H. E. Green, *IEEE Transactions on Microwave theory and Techniques* **13**, 676 (1965).
- [53] H. N. Dawirs, *IEEE Transactions on Microwave Theory and Techniques* **17**, 127 (1969).
- [54] P. Y. Wong, Y. Lau, D. Chernin, B. W. Hoff, and R. M. Gilgenbach, *IEEE Transactions on Electron Devices* **65**, 710 (2018).
- [55] G. Guillermo, *Microwave Transistor Amplifiers* (Prentice Hall, NJ, USA, 1984).
- [56] J. G. Wohlbiel, J. H. Booske, and I. Dobson, *IEEE Transactions on Plasma Science* **30**, 1063 (2002).
- [57] C. K. Chong, J. A. Davis, R. H. Le Borgne, M. L. Ramay, R. J. Stolz, R. N. Tamashiro, J. P. Vaszari, and X. Zhai, *IEEE Transactions on Electron Devices* **52**, 653 (2005).
- [58] D. K. Abe, M. T. Ngô, B. Levush, T. M. Antonsen, and D. P. Chernin, *IEEE transactions on plasma science* **28**, 576 (2000).
- [59] V. Srivastava and S. Joshi, *IETE Technical Review* **6**, 500 (1989).
- [60] D. Chernin, T. Antonsen, B. Levush, and D. R. Whaley, *IEEE Transactions on Electron Devices* **48**, 3 (2001).
- [61] C. L. Kory, *IEEE Transactions on Electron Devices* **48**, 1718 (2001).
- [62] S. Datta, P. Jain, M. R. Narayan, and B. Basu, *IEEE Transactions on Electron Devices* **45**, 2055 (1998).
- [63] D. Dialetis, D. Chernin, T. M. Antonsen, and B. Levush, *IEEE transactions on electron devices* **56**, 935 (2009).
- [64] V. Srivastava, *IETE journal of research* **49**, 239 (2003).
- [65] H. Freund, *IEEE transactions on plasma science* **28**, 748 (2000).
- [66] S. Sensiper, (1951).
- [67] M. A. Othman, V. A. Tamma, and F. Capolino, *IEEE Transactions on Plasma Science* **44**, 594 (2016).
- [68] M. A. Othman, F. Yazdi, A. Figotin, and F. Capolino, *Physical Review B* **93**, 024301 (2016).
- [69] A. F. Abdelshafy, M. A. Othman, F. Yazdi, M. Veysi, A. Figotin, and F. Capolino, *IEEE Transactions on Plasma Science* **46**, 3126 (2018).
- [70] A. F. Abdelshafy, M. A. Othman, A. Figotin, and F. Capolino, *High Power Microwave Sources and Technologies Using Metamaterials* , 17 (2021).
- [71] A. Figotin, *Journal of Mathematical Physics* **62** (2021).
- [72] A. F. Abdelshafy, F. Capolino, and A. Figotin, *arXiv preprint arXiv:2201.01712* (2022).

- [73] A. Figotin, *Journal of Mathematical Physics* **63** (2022).
- [74] A. Figotin, *Journal of Mathematical Physics* **64** (2023).
- [75] G. Branch and T. Mihran, *IRE Transactions on Electron Devices* **2**, 3 (1955).
- [76] S. K. Datta and L. Kumar, *IEEE transactions on electron devices* **56**, 1344 (2009).
- [77] S. Ramo, *Proceedings of the IRE* **27**, 757 (1939).
- [78] T. Antonsen and B. Levush, *IEEE transactions on plasma science* **26**, 774 (1998).
- [79] R. G. Hutter, *Beam and wave electronics in microwave tubes* (Van Nostrand, 1960).
- [80] P. Y. Wong, D. Chernin, and Y. Lau, *IEEE Electron Device Letters* **39**, 1238 (2018).
- [81] A. Figotin and G. Reyes, in *High Power Microwave Sources and Technologies Using Metamaterials* (Wiley Online Library, 2021) pp. 57–85.